

INVESTIGATING BEHAVIOUR OF ELASTOMERIC BEARINGS
CONSIDERING NON-STANDARD TOP AND BOTTOM BOUNDARY
ROTATIONS

INVESTIGATING BEHAVIOUR OF ELASTOMERIC BEARINGS
CONSIDERING NON-STANDARD TOP AND BOTTOM BOUNDARY
ROTATIONS

By RICHARD DARLINGTON, B.ENG & MGMT

A Thesis Submitted to the School of Graduate Studies in Partial Fulfilment of the
Requirements for the Degree Master of Applied Science

McMaster University

© Copyright by Richard Darlington, December 2019

MASTER OF APPLIED SCIENCE (2019)

(Civil Engineering)

McMaster University

Hamilton, Ontario

TITLE: Investigating Behaviour of Elastomeric Bearings
Considering Non-Standard Top and Bottom
Boundary Rotations

AUTHOR: Richard Darlington, B. Eng. & Mgmt

SUPERVISOR: Dr. Mike J. Tait

CO SUPERVISOR: Dr. Tracy C. Becker

NUMBER OF PAGES: xi, 62

LAY ABSTRACT

Seismic isolation, in which a flexible layer is used to separate a structure from the ground below, is a proven method for reducing earthquake demands that has been recently introduced into Canadian building code. Typical installations of seismic isolation use rigid diaphragms to bound the end plates of the isolators, which is more easily implemented in new build scenarios but requires extensive excavation and foundation work in retrofit applications. An alternative form of isolation involves placing the isolation plane on top of first floor columns, potentially resulting in flexible boundary conditions. To address this, an experimental program on a quarter-scale column-top isolation system was conducted to investigate how rotations of both top and bottom bearing end plates impact key design assumptions such as horizontal stiffness, rotational stiffness, and stability. This research can help to expand the number and types of buildings isolation can be applied to, creating more resilient communities.

ABSTRACT

Seismic isolation, in which a flexible layer is used to separate a structure from the ground below, is a proven method for reducing earthquake demands that has been recently introduced into the 2015 Canadian building code. Typical installations of seismic isolation use rigid diaphragms to bound the end plates of the isolators, which is easily implemented in new build scenarios but requires extensive excavation and foundation work in retrofit applications. An alternative form of isolation involves placing the isolation plane on top of first floor columns, potentially resulting in flexible boundary conditions. There have been very few experimental programs that mimic these flexible boundary conditions.

To address conditions that may be found in column-top isolation design schemes, such as flexible framing and lightly axially loaded corner bearings, an experimental program on a quarter-scale column-top isolation system was conducted. The goals of the investigation were to investigate how rotations of both top and bottom bearing end plates impact key design assumptions such as horizontal stiffness, rotational stiffness, and stability, and how these effects change with axial load.

Experimental findings showed that flexible boundary conditions reduce horizontal stiffness based on the sum of rotation at the ends, regardless of the rotation of one bearing end plate with respect to the other. This decrease is dependent on axial load, with more axial load leading to a higher decrease in horizontal stiffness. The rotational stiffness significantly decreases with bearing shear strain and models that use linear, elastic rotational springs underrepresent

rotations at the boundaries. Lastly, traditionally used design limits for stability can be used for bearings of moderate shape factor ($S_1 = 19.6$ used in testing) bounded by flexible framing, but these theoretical limits can overestimate the experimental determined limits by nearly double for bearings of low shape factors ($S_1 = 7.9$ used in testing).

ACKNOWLEDGEMENTS

I would like to thank my supervisor, Dr. Tracy Becker for giving me the opportunity to work with her and help me realize my personal and professional goals through her support, guidance, and commitment. I would also like to thank my co-supervisor, Dr. Mike Tait, for taking me on and providing key advice during my experimental work.

I would like to thank Kent Wheeler who helped me problem solve and plan during my time in the lab, keeping me sane through the obstacles and trials that come with experimental work. I would also like to thank Paul Heerema who was always engaged in my project, always brought a yes man attitude, and shared many laughs with me in an otherwise windowless environment.

To my friends and housemates, Matt East, Dan LeeKim, Kevin McNamara, and Paul Stenecker, the real graduate degree is the friends we made along the way.

This work would not have been possible without the love of my parents, grandparents and brother, who have always been my greatest support.

Finally, to my intrepid partner Iwona, thank you for agreeing to join me on the west coast to build a new life together and supporting me through this degree.

TABLE OF CONTENTS

LIST OF FIGURES	viii
LIST OF TABLES	x
LIST OF SYMBOLS	xi
1 INTRODUCTION	1
1.1 Seismic Isolation in Canada	1
1.2 Literature Review of Elastomeric Bearings	7
1.3 Problem Statement	13
2 EXPERIMENTAL PROGRAM	15
2.1 Response of the Natural Rubber Bearing Assemblies	23
2.1.1 <i>Pure Rotation</i>	23
2.1.2 <i>Cyclic shear and rotation</i>	24
2.1.3 <i>Larger strain testing</i>	33
2.1.4 <i>Comparison with simplified models</i>	37
2.2 Response of the Lead Rubber Bearing Assemblies	41
2.2.1 <i>Pure rotation</i>	41
2.2.2 <i>Cyclic testing</i>	42
3 CONCLUSIONS AND RECOMMENDATIONS	49
3.1 Conclusions	49
3.2 Recommendations for Future Work	51
4 REFERENCES	53

LIST OF FIGURES

Figure 1-1: (a) Conventional base isolated and (b) Column-top isolated structure.....	3
Figure 1-2: Potential displaced shape of isolated structures with flexible framing.....	3
Figure 1-3: Strathcona Elementary column-top isolation scheme and flexible mechanical connections	4
Figure 1-4: Vancouver Schools Age by Decade.....	6
Figure 2-1: Column-Top test setup with NRB and HSS127x127x8.0 column.....	15
Figure 2-2: Schematic drawing of the experimental system.....	16
Figure 2-3: (a) Single-action actuators and pin connection (b) Rotation instrumentation	18
Figure 2-4: (a) Displacement protocol (b) Bearing positive notation.....	21
Figure 2-5: Comparison of theoretical buckling loads to testing protocol shown between 200 and 400% shear strain	22
Figure 2-6: Pure rotation test at +0.02 rad of top rotation	23
Figure 2-7: Bearing top moment-rotation (Left), bottom moment-rotation (Centre), and shear-rotation (Right) curves for the NRB pure rotation test under two axial load cases	24
Figure 2-8: Shear-Shear strain, top and bottom moment-rotation responses of column subassemblies at 5 MPa axial load (100 kN)	25
Figure 2-9: (a) NRB-102x102x8.0 with $\theta_{top} = 0$ (b) NRB-102x102x8.0 with $\theta_{top} = 0.02$ rotation, (c) NRB-76x76x4.8 with $\theta_{top} = 0$, (d) NRB-76x76x4.8 with $\theta_{top} = 0.02$	26
Figure 2-10: Bearing stiffness decrease with total rotation, θ_{total} , at 100% shear strain and (a) 5 MPa and (b) 2.5 MPa compared against HSS127x127x8.0 with rigid top conditions	29
Figure 2-11: Bearing stiffness decrease with axial pressure at 100% shear strain and $\theta_{top} = 0$ rad, compared against HSS127x127x8.0 with rigid top conditions at 2.5 MPa.....	30
Figure 2-12: Comparison of global NRB stiffnesses at varied loads and applied top-plate rotation	31
Figure 2-13: NRB tested to 300% shear strain supported by the 102x102x8.0.....	33
Figure 2-14: Monotonic shear-strain and bottom bearing moment-rotation curves for 127x127x8.0 (left) and 102x102x8.0 (right) subassemblies.....	34
Figure 2-15: Behaviour pre and post extreme loading scenarios, 5 MPa	36
Figure 2-16: Force-displacement, top and bottom moment-rotation responses of the modelled vs experimental column subassemblies at 5 MPa axial load (100 kN).....	39
Figure 2-17: Comparison of Equation 2-5 with the NRB moment-rotation curves due to applied moment.....	41
Figure 2-18: Bearing top moment-rotation (Left), bottom moment-rotation (Centre), and shear-rotation (Right) curves for the LRB pure rotation test under two axial load cases.	42
Figure 2-19: Shear-Shear strain, top and bottom moment-rotation responses of column subassemblies at 2 MPa axial load (80 kN)	43

Figure 2-20: (a) NRB-102x102x8.0 with $\theta_{top} = 0$ rad (b) NRB-76x76x4.8 with $\theta_{top} = 0$ rad	45
Figure 2-21: Comparison of LRB stiffnesses at varied pressures and applied top-plate rotation	46
Figure 2-22: Comparison of Equation 2-5 with the LRB moment-rotation curves due to applied moment.....	48

LIST OF TABLES

Table 2-1: Column properties	19
Table 2-2: Bearing properties	20
Table 2-3: Global NRB secant stiffness comparisons at 100% shear strain	27
Table 2-4: Local bearing secant stiffness comparisons at 100% shear strain under 5 MPa	28
Table 2-5: Secant stiffnesses (N/mm) at 300% shear strain at varied load levels	35
Table 2-6: Secant stiffnesses (N/mm) at 100% shear strain at varied load levels	36
Table 2-7: Global LRB specimen secant stiffness comparisons at 40% shear strain	45

LIST OF SYMBOLS

A	Area of rubber
D	Diameter of rubber bearing
EI_{eff}	Effective flexural stiffness
G	Shear modulus of rubber
h	Height of isolator
I	Second moment of area
K_{eff}	Effective (secant) stiffness of bearing
$K_{bearing}$	Horizontal stiffness of a bearing
K_{column}	Horizontal stiffness of a column
K_{rm}	Instantaneous rotational stiffness
K_{rm0}	Rotational stiffness at zero shear strain
L	Length of supporting column
M_{bot}	Moment at the bearing bottom plate
M_{top}	Moment at the bearing top plate
P_{crit}	The critical load at which instability occurs
Q_d	Characteristic strength of isolator
r	Radius of rubber
r_{lc}	Radius of lead core
SR	Stiffness ratio between a bearing and supporting column
S_1	The primary shape factor of a bearing - Aspect ratio of a rubber layer
S_2	The secondary shape factor of a bearing - Aspect ratio of the bearing
t	Thickness of a single rubber layer
t_r	Total thickness of rubber across the height of an isolator
t_s	Thickness of a single steel shim
x	Applied horizontal displacement
Δ	Displacement of bearing
γ	Shear strain of bearing
θ_{bot}	Rotation of the bearing bottom plate
θ_{local}	Rotation of the bearing top plate with respect to the bottom plate local axis
θ_{total}	Magnitude of rotation at the bearing top and bottom plates
θ_{top}	Rotation of the bearing top plate

1 INTRODUCTION

1.1 Seismic Isolation in Canada

The original concept of isolation was introduced in the 1950s to allow for thermal expansion in highway bridges and suppression of acoustic vibration, but the modern use of isolation as a form of seismic control was introduced in the early 1970s with the construction of the William Clayton building in New Zealand (Skinner et al., 1992). Isolators are flexible in the horizontal direction using either sliding surfaces or rubber but are stiff in the vertical direction to carry the weight of the superstructure. For rubber bearings, the high vertical stiffness is achieved through bonded steel plates restraining the bulging of rubber (France Patent No. 1.110.285, 1954). Using isolators, the natural period of a structure is lengthened, often beyond the predominant frequency content of an earthquake. As a result, the seismic demand on a structure can be significantly reduced, resulting in increased resiliency by reducing risk of damage to structural and non-structural components. This allows for continued operation after a major earthquake.

Canada has recently introduced isolation as a codified method of structural control in the 2015 National Building Code of Canada (NRCC, 2015), opening the door for new Canadian construction projects to employ isolation technology. Base isolation can be installed in new build scenarios, where the cost of installation is estimated as roughly 5% of the total construction cost (Kelly & Konstantinidis, 2011). Unfortunately, some structures designed to older and less stringent building codes are at risk of significant damage or even collapse in large scale earthquakes, resulting in potentially devastating economic repercussions and loss of life (Kunnath et al., 1995). Earthquakes in the two

major seismic regions of Canada, the coast of British Columbia and the Quebec City-Montreal-Ottawa corridor, could cost as much as \$75 billion and \$61 billion, respectively (Insurance Bureau of Canada, 2016). To combat this, many Canadian structures should be retrofit or rebuilt. Retrofitting using isolation at the base of the structure is typically reserved for high importance structures with significant budgets such as the San Francisco City Hall isolation seismic retrofit, which costed \$220 million. (San Francisco Public Works, n.d.). Installation of base isolation in existing structures is expensive due to the costs of excavation, foundation work, and construction of a rigid diaphragm. This cost severely limits the types and number of structures in which isolation may feasibly be employed.

To address these large costs and expand the types of buildings that isolation retrofit strategies can be applied to, an alternative form of isolation can be used where a combination of elastomeric isolators and flat sliders is used to isolate the mass above the first-floor columns, as shown in Figure 1-1. Locating the isolation layer on top of the first-floor columns can mitigate many of these costs (Matsagar & Jangid, 2008) but results in atypical conditions that must be accounted for. One of the main differences between this application and typical base isolation is that column-top isolation can be bounded by flexible framing, potentially allowing the bearing end plates to rotate. This is compared to traditional applications of isolation, where parallel and unrotated top and bottom end plates are assumed.

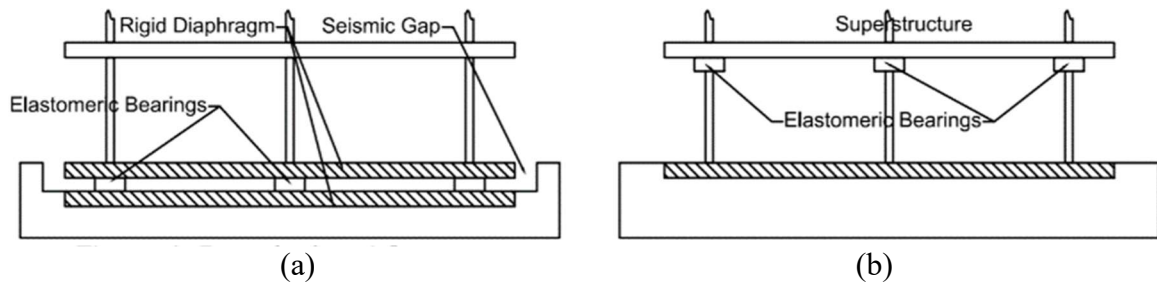


Figure 1-1: (a) Conventional base isolated and (b) Column-top isolated structure

This implementation results in a similar subassembly as seen in isolated bridges in which the bearing is located at the top of the pier. If the columns or piers below the bearings, or the diaphragm or bridge deck above, are not rigid, the bearings installed may experience rotations at one or both ends of the isolator as shown in Figure 1-2, potentially affecting isolator design criteria such as bearing buckling and horizontal stiffness, which are largely based on analytical models and experimental tests that do not account for the effects of boundary rotation.

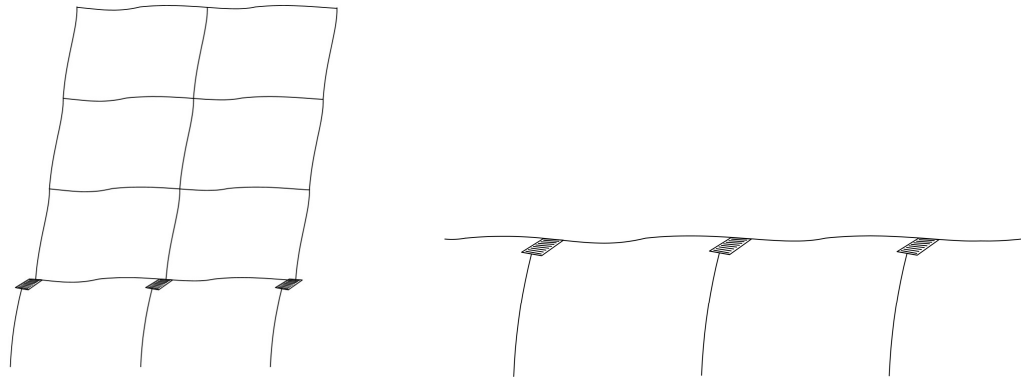


Figure 1-2: Potential displaced shape of isolated structures with flexible framing

Column-top isolation has been employed in projects such as the Main Building of the Shimizu Institute of Technology in Japan (Tamura et al., 2004), the Christchurch Justice and Emergency Services Precinct in New Zealand (Pettinga & Oliver, 2015), and recently,

in the retrofit of the heritage designated Strathcona Secondary School building located in Vancouver, British Columbia (Kurucz, 2018). A 120-year-old masonry wall school building was retrofitted with lead rubber bearings and flat Teflon sliders, with architectural and mechanical details to accommodate up to 250 mm of displacement. The isolation plane was located above the first-floor columns, where the exterior walls were saw-cut. Mechanical connections were replaced with flexible connections, as can be seen in Figure 1-3 (Ausenco, 2017). In these projects, very large columns are used to support the isolators and minimize the rotation at the bearing end plate.



Figure 1-3: Strathcona Elementary column-top isolation scheme and flexible mechanical connections

This project was completed with a budget of \$25.6 million, which also included significant architectural and educational upgrades. The isolation retrofit required additional engineering peer review time and costs because the method was not codified under the Seismic Retrofit Guidelines (SRG) (APEGBC, 2017) followed for BC schools (Sherstobitoff, 2018). Thus, to expand the number and types of structures to which

advanced structural can be used, development and improvement of cost-effective and codified retrofit methods is critical to improving community resilience to seismic events and preserving heritage.

The implementation of isolation in the Strathcona heritage project represents a shift in Canadian seismic retrofit strategies, where performance past life safety and use of advanced structural control can be desirable. Unfortunately, one pressing issue in British Columbia is the number of at-risk schools requiring major retrofit or rebuild in order to meet life-safety requirements. The British Columbia (BC) Ministry of Education (MOE) manages a portfolio of 1600 provincial public schools, of which 750 are in high risk seismic areas (Ventura et al., 2017). Roughly 45% of the schools located in high hazard areas are defined as high risk as they are constructed without adequate ductility or detailing according to modern building code provisions. Figure 1-4 summarizes the number of extant schools in only Vancouver, where the average age is 73 years – long before building codes began to address seismic concerns (Commonwealth Historic Resource Management Limited, 2007). Many of these schools were built prior to 1930 and have significant heritage value. In 2004, the Seismic Mitigation Program (SMP) was created to address the problem of aging and insufficient school infrastructure against a growing concern of unpreparedness for large-scale seismic events, where almost \$2.5 billion has been spent or allocated since 2004 (Government of British Columbia, 2019). To address this critical issue, a set of retrofit guidelines were developed to minimize cost and standardize both the assessment of seismic performance and approach to structural retrofit (APEGBC, Structural Engineering Guidelines for the Performance-based Seismic Assessment and

Retrofit of Low-Rise British Columbia School Buildings - 1st Edition (SRG1), 2011). Since the inception of the SMP, only half of the high-risk schools have been retrofitted or reconstructed and the original \$1.5 billion budget surpassed, demonstrating the need for more cost-effective retrofit solutions (VSB, 2019).

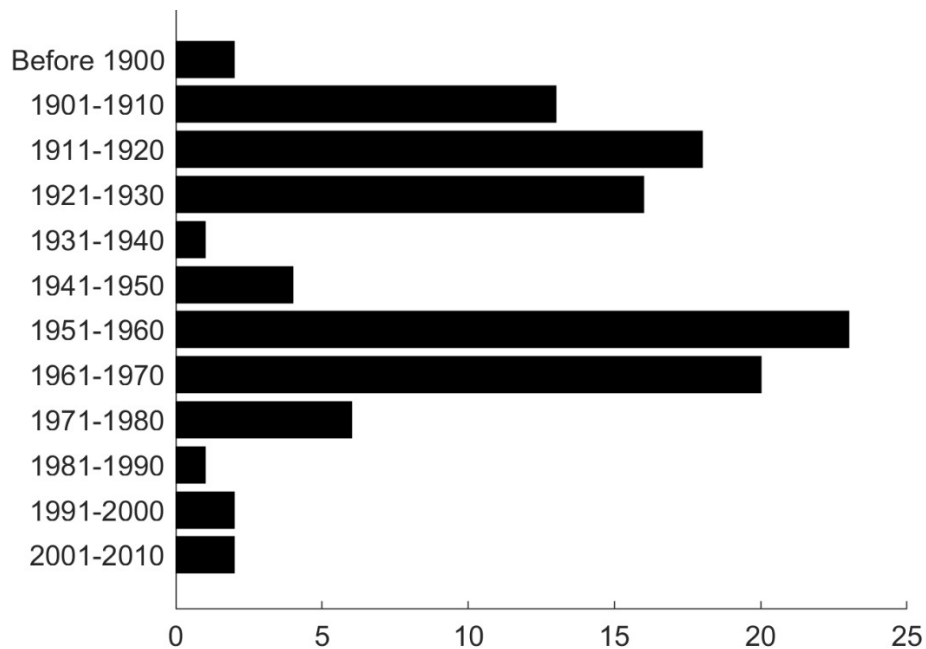


Figure 1-4: Vancouver Schools Age by Decade

The goal of the seismic retrofit guidelines is to elevate all school structures to life-safety levels of performance as quickly and cost-effectively as possible due to the number of schools requiring retrofit. As a result, retrofit guidelines leave little room for advanced protective structural systems such as damping or isolation due to long peer-review times and advanced design work, with exceptions only being made when the building is of “Class A” or primary heritage significance. A study commissioned by the Vancouver School Board (VSB) in 2007 proposed a list of 64 school sites deserving special consideration in

the seismic mitigation process (Commonwealth Historic Resource Management Limited, 2007). Only Strathcona Elementary school out of the recommended 64 heritage schools was considered for retrofit using isolation. Schools that are deemed a lower class of heritage (B or C) are not protected and are at risk of being demolished without creative and cost-effective forms of seismic retrofit (City of Vancouver, 2014). The risk of demolishing and rebuilding heritage structures are compounded as only 20% of school facilities in Vancouver are considered in fair or better condition, requiring an estimated \$761 million in deferred maintenance costs (Vancouver School Board, 2019). With such high levels of deferred maintenance, demolition is often the most viable economic recourse, resulting in a significant loss of heritage value. Column-top isolation represents an opportunity to preserve heritage and elevate the performance of school structures above life-safety, but more experimental work on the behaviour of elastomeric bearings in these applications are required to establish how flexible boundaries can affect design limitations and modelling.

1.2 Literature Review of Elastomeric Bearings

Elastomeric isolators use alternating layers of bonded rubber and steel to provide low horizontal stiffness (a flexible layer) and sufficient vertical stiffness to carry the weight of the structure above. The horizontal stiffness and vertical stiffness are two of the main design concerns for an isolation system, as the former determines the displacement and forces in the structures, and the latter contributes to stability. In some types of elastomeric bearings, additional damping is incorporated into the bearing at the isolation level. The natural rubber bearing (NRB) or low-damping rubber bearing is the most basic form of manufactured elastomeric bearing and is generally approximated with linear behaviour. Lead-core rubber

bearings (LRB) include a yielding lead core confined by annular layers of elastomer and steel (Naiem & Kelly, 1999). This yielding lead core provides an initial horizontal stiffness, which is desirable to prevent lateral movement from wind, and hysteretic energy dissipation, which helps to limit displacement during an earthquake ground motion. Both an NRB and LRB were tested in the experimental program detailed in Section 2.

While the horizontal and stability behaviour of these isolators is quite complex, design and analysis are typically based on simplified mechanical behaviour and experimental testing where the bearing end plates are bounded by rigid diaphragms. This may be suitable in typical installations of isolation, but for scenarios where rotation may be present, such as when bounded by flexible framing in a column-top isolation setup, there is very little experimental data with similar conditions. As a result, current models may not properly account for the influence of rotation on the horizontal behaviour of elastomeric isolators, especially simplified models used in analysis and design. To explore this further, a literature review is presented on stability of elastomeric bearings, the current state of elastomeric bearing modelling, and lastly, experimental and analytical research on bearings with rotated boundary conditions.

The basis of many studies in these areas comes from the differential equations proposed by Haringx (Haringx, 1949). Haringx worked to quantify the buckling load of shear-flexible short rubber vibration isolators based on Euler's buckling load, proposing a set of differential equations where both shear and flexural deformations are considered, requiring displacement and rotation boundary conditions at the ends of the bearing. These differential equations were used to describe the mechanical behaviour of the rubber column

when subjected to combined axial load and shear displacement. Gent (1964) then applied Haringx's theory to multilayered (laminated) rubber compression blocks, thus exploring the influence of axial load on the static horizontal stiffness. Gent (1964) substituted the bending and shear stiffnesses of a homogenous rubber column used by Haringx for the bending and shear stiffnesses based on a single layer of rubber, confined by steel pads, smeared over the height of the bearing. Gent (1964) conducted experimental research on these multilayer blocks with rigid boundaries, finding that Haringx's theoretical work satisfactorily captures the critical load and static shear stiffness under various loading conditions in its undeformed state. Gent (1964) further concluded that increasing axial load on a bearing results in decreased horizontal stiffness. The works of Gent (1964) and Haringx (1949) would establish the basis of modern isolation.

Buckle and Kelly (1986) experimentally tested more modern elastomeric bearings and proposed an equation to capture this decrease in horizontal stiffness with axial load, where the stiffness reaches zero (stability limit) as axial load approaches the buckling load. Buckle and Liu (1993) then proposed an equation to capture the decrease in buckling load as a function of the overlapped area until the deformation of the bearing was equal to its diameter. This reduction in buckling load was shown to be an overly conservative estimate by experimental tests (Buckle et al., 2002, Sanchez et al., 2013). Warn et al. proposed a minimum vertical stiffness, making the Buckle and Liu (1993) equation a piecewise function, which is commonly used today to design isolation systems (Warn et al., 2007, Buckle & Liu, 1993). All of these experimental tests were conducted using rigid end conditions of the bearing. These limits cannot be reliably used for design or analysis of

bearings with flexible end conditions. There exists a gap in experimental research done on bearings with rotated boundary conditions. This also influences the modelling of bearings, as models can underrepresent or omit the effects of rotation on the behaviour of bearings without backing experimental data.

Many isolation models are derivations of Haringx theory, which requires boundary conditions to solve. Typically, rotation boundary conditions are rigid, and the mathematical models are defined as such. Koh and Kelly initially used Haringx theory to derive an exact viscoelastic model with an infinite series of complex numbers (Koh & Kelly, 1987). To make models easier to integrate into structural analysis programs, mechanical representations of isolation models were developed as well. Koh and Kelly then proposed a linear two spring mechanical model, with a shear and flexural spring to predict horizontal behaviour of bearings and capture $P-\Delta$ effects (Koh & Kelly, 1988). This model showed good agreement with the exact viscoelastic model and was verified by experiments bounded by rigid end plates. This two-spring model, refined by Kelly to include rotational springs at both the top and bottom boundaries of the element connected with rigid links to a mid-height shear spring, has been built upon by many researchers (Kelly J. M., 1997).

Nagarajaiah and Ferrell extended the Koh and Kelly mechanical model to include non-linear rotational springs at the bottom and top of the bearings with rigid links connected to a non-linear shear spring, capable of predicting post buckling behaviour but calibrated based on limited test results (Nagarajaiah & Ferrell, 1999). Kikuchi et al. developed a 3-dimensional model using non-linear axial springs, similar to fiber elements in columns, in place of rotational strings to capture the effects of varying axial load on horizontal stiffness

and stability (Kikuchi et al., 2010). Han and Warn developed a mechanistic model using non-linear axial springs (similar to the Kikuchi model) requiring only material parameters without relying on experimental calibration (Han & Warn, 2014). Han and Warn concluded that the critical behaviour of isolators at large shear strains is largely controlled by the non-linear moment-rotation properties, and not just overlapped area. Kumar et al. (2014) developed a model that captured characteristics for beyond design basis earthquakes that incorporates important considerations such as decrease in buckling load with shear strain, decrease in horizontal stiffness with shear strain, and added cavitation and post cavitation behaviour. These decreases are considered explicitly from empirical equations instead of incorporating P- Δ effects in the stiffness matrix. In general, the models presented have not addressed or been experimentally verified with rotated boundary conditions. It was not until recently that models with rotated boundary conditions were being considered as isolation was applied in novel design strategies and retrofit applications.

Karbakhsh Ravari et al. (2012) derived movement and rotation equations for a multilayer elastomeric bearing considering constant boundary rotations based on Haringx theory, finding that the horizontal stiffness is decreased for bearings with rotated end conditions and the magnitude of decrease changes with axial load. Thus, boundary rotation is relevant during analysis, especially for column-top isolated structures where axial loading can vary with tributary area. In a similar formulation, Crowder and Becker (2017) developed and implemented a shear-rotation coupled stiffness matrix model for NRBs based on the single layer stiffness model of Chang (2002). While these models can account for changes in bearing stiffness under typical displacements, they do not capture more

extreme behaviour. Rastgoo Moghadam and Konstantinidis (2017) compared the Nagarajaiah and Ferrell (1999), Iizuka (2000), and Han and Warn (2014) mechanical spring models and modified the Han and Warn model to account for constant support rotation and compared the buckling loads against finite element analysis. Ishii et al. (2017) extended the Kikuchi-Aiken mechanical spring model to capture the asymmetric bending moment associated with rotated boundaries, showing agreement with the experimental program included in the paper, but with decreasing accuracy as shear strain increased. They also concluded that a mechanical model that uses non-linear axial springs accounting for overlapped area can adequately capture changes in the rotational stiffness with shear strain.

Similar to modeling, experimental testing on the horizontal behaviour of elastomeric bearings has largely been conducted using parallel end conditions, and thus, design values are typically informed by experimental testing that does not necessarily represent the end conditions present with flexible framing. However, Ishii et al. (2017) investigated the moment-rotational behaviour by applying cyclic rotations at pre-applied constant shear strains. They found that bearing rotational stiffness increases with increasing vertical load but decreases with increasing shear strain. In an opposite approach, Rastgoo Moghadam (2017) tested an NRB with a constant single end plate rotation, representative of settlement or installation errors. They concluded these constant rotations can impart initial forces, shifting the hysteretic loops where the magnitude of shift is influenced by axial loads. Chen et al. (2019) tested full-scale high damping rubber (HDR) bearings under multiaxial excitation including pitch, roll, and yaw demands. The peak rotations used in the study were 0.0043 rad, slightly amplified from the maximum measured values in full scale

building tests with rigid diaphragms bounding the isolation plane (Chen et al, 2016). While the effects of the rotations on horizontal stiffness were less than 5%, the rotations incorporated were representative of typical application rather than in the column-top configuration. However, none of these experiments simulated the combinations of demands that would arise from flexible framing bounding the bearing.

Crowder and Becker (2017) considered the horizontal behaviour of a column-top elastomeric isolation system with various columns of decreasing stiffness and concluded that flexible boundary conditions can significantly reduce the horizontal stiffness of the bearing. The experimental program of Crowder and Becker (2017), which only included NRBs did not consider rotation at the top of the bearing or investigate the effect of axial loading. The experimental program presented in this study explores these gaps using NRB and LRB on a column-top isolation system with varied applied top plate rotations with multiple axial load levels. This program provides insight and experimental data for future applications of bearings experiencing double end plate rotation at high shear strains. This will allow for well considered design when bearings are bounded by flexible framing. To assess if currently widely available elastomeric bearing models are sufficient for analysis of column-top isolation systems, a comparison with existing models is presented.

1.3 Problem Statement

With the information presented, some conclusions can be drawn about the state of Canadian structures in high seismicity zones and the steps required to implement column-top isolation as a retrofit strategy.

1. There are many deficient and community-critical buildings in Canada's high seismicity zones that were built before codes focused on earthquake demands were introduced. Many of them have significant heritage value, require maintenance, and are at risk of being demolished.
2. Column-top isolation presents a non-intrusive method of reducing seismic demands, maintaining heritage value and it has already been used once in Canada to preserve the heritage of a 120 year old school structure.
3. Flexible boundaries may be present in column-top isolation retrofits resulting in atypical conditions not previously explored experimentally. The impacts of these flexible boundaries on horizontal stiffness, rotational stiffness, and stability must be explored for proper design, analysis, and implementation of column-top isolation systems.
4. Many models can capture rotations at the boundaries but do not consider the effects on horizontal behaviour and have not been experimentally verified with rotation.

The research in this work aims to address the gap in experimental knowledge to expand column-top isolation as a retrofit strategy. A quarter-scale experimental program with NRBs and LRBs was conducted to assess the influence of rotation of both bearing end plates on the horizontal behaviour of a column-top isolation system. The effect of axial load was also investigated. Results from this experimental program were then compared to currently available mechanical models (Crowder & Becker, 2017), (Kumar et al., 2015) in OpenSEES (McKenna & Fenvez, 2006) to determine if currently available models are sufficient for design and analysis of bearing systems with flexible framing

2 EXPERIMENTAL PROGRAM

To assess the effects of top and bottom plate rotation and large shear strain on the horizontal behaviour of elastomeric bearings in a column-top isolation system, a quarter-scale experimental program was conducted at the Applied Dynamics Laboratory at McMaster University. The test setup, shown in Figure 2-1 includes two vertical double-action actuators to apply axial load to the system (located at the ends of the green loading beam), two single-action actuators to apply rotation to the bearing top plate, and a horizontal double-action actuator with linear rails at the base of the column to apply up to +/- 100 mm of displacement. Modifications were made to the quarter-scale column-top isolation test setup designed by Crowder and Becker (2017) in order to control rotations at the top of the bearing and capture the associated shear forces and moments.

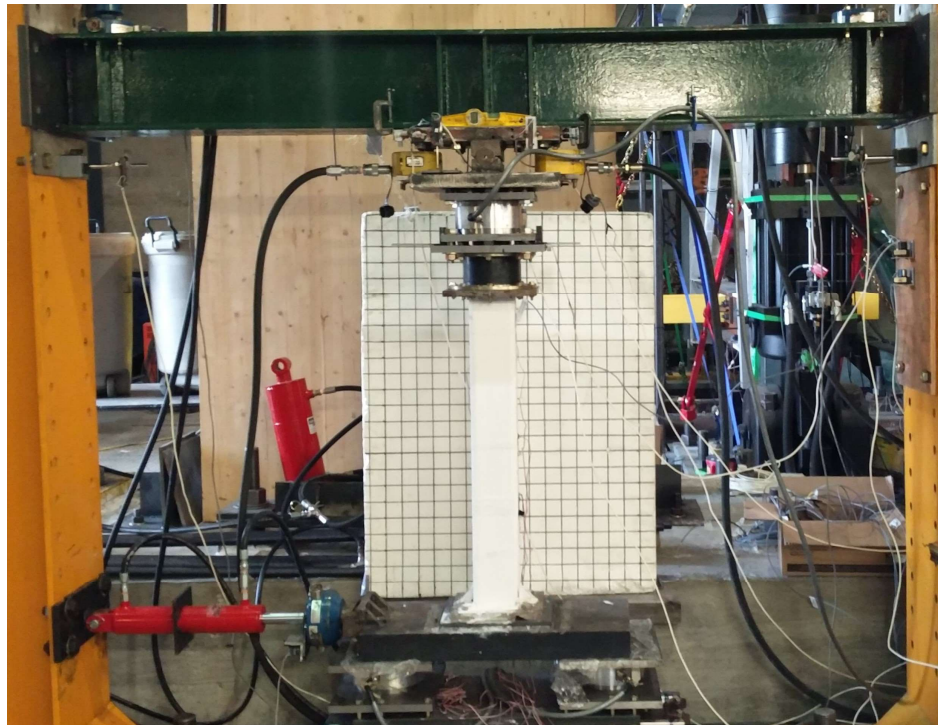


Figure 2-1: Column-Top test setup with NRB and HSS127x127x8.0 column

The schematic of the experimental setup is presented in Figure 2-2. Displacement, rotation, force, and moment measurements were collected through a series of string and linear potentiometers (L-Pot), rotation variable differential transformers (RVDT), single degree of freedom (SDOF) load cells, 6 degree of freedom (6DOF) load cells, and strain gauges. The 6DOF load cell on the top of the bearing was used to measure shear and moment at the bearing top plate, as well as control for axial load. Moment at the bottom of the bearing plate was measured using strain gauges placed along the column sides, converting strain into force couples.

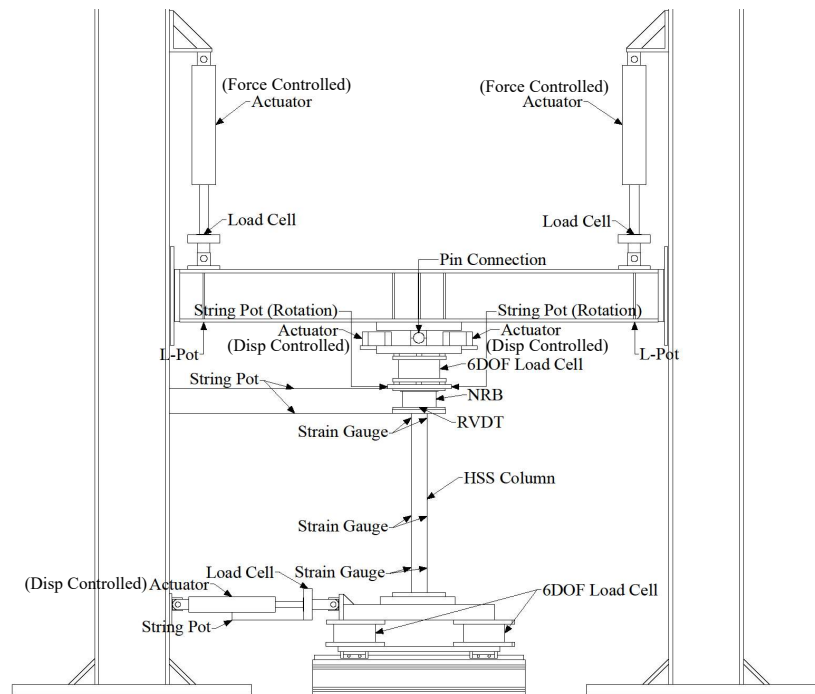


Figure 2-2: Schematic drawing of the experimental system

The strain gauges were placed in three pairs along the column to form a full bending moment diagram along the column. If the column was yielded from testing, the residual moment at the top of the column was removed from the data in post processing.

Instrumentation used for data collection were isolated from instrumentation used for actuator control for safety.

Two pinned vertical actuators connected to reaction columns were used to apply vertical load to the system through the loading beam. These vertical actuators were force controlled by summing the two and maintaining a constant load at the 6DOF load cell above the isolator. Planarity of the loading beam between the two actuators was then maintained using linear potentiometers placed directly underneath the left and right vertical actuator connection points. These linear potentiometers were also used for displacement control to control vertical movement of the loading beam, which allowed for test specimens to be exchanged quickly. The loading beam was bounded by low friction interfaces which transferred horizontal load through bearing onto the reaction column and reduced the losses of vertical load due to friction. Despite losses due to friction being mostly negligible, axial load was force controlled through the 6DOF load cell on top of the bearing to ensure consistent application of load. In order to apply horizontal displacement, the horizontal actuator at the base of the setup was displacement controlled using a string potentiometer. The capabilities of the horizontal actuator are limited to quasi-static testing. Due to the quasi-static limitations of the setup, dynamic effects such as strength degradation due to heating of the LRB core cannot be captured (Kalpakidis et al., 2010).

The most notable change to the system was the inclusion of a controlled pin connection at the top of the bearing, as shown in Figure 2-3a. The connection is capable of allowing rotation and transmitting shear but only resists axial load in bearing and thus, provides no tension resistance. The force-couple that controlled rotation of the bearing top

plate was applied using two paired single-acting vertical actuators and was displacement controlled through a rotation calculation between two string potentiometers. This rotation calculation was compared against a rotation sensor attached to the bearing top plate as shown in Figure 2-3b. The rotation sensor was not used for control due to the error range of the sensor, as well as its sensitivity to acceleration and was not used for the results as accelerations caused unpredictable spikes in the data. Through these modifications, it was possible to test the setup with rigid connection conditions (when the actuators hold the top plate at zero rotation) and any pre-specified rotation angles.

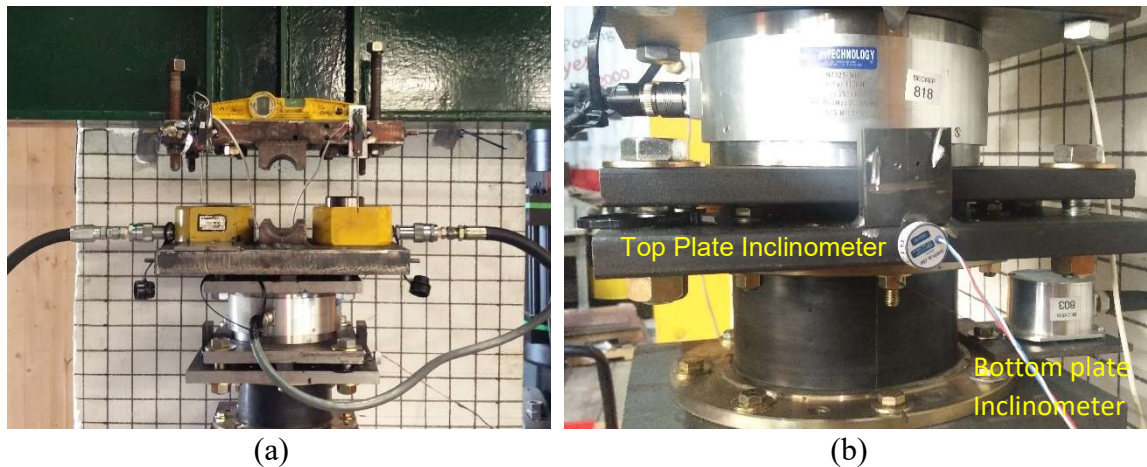


Figure 2-3: (a) Single-action actuators and pin connection (b) Rotation instrumentation

Three column types with heights of 0.875m were selected based on the work of Crowder and Becker (2017). The two stiffest columns were designed to stay elastic during cyclic testing while the smallest column was designed to yield. The properties of the columns can be found in Table 2-1. These column types support an NRB and an LRB. The manufacturers drawings for these bearings can be found in Appendix A. While the bearings have similar horizontal stiffness, the LRB is larger and more slender with almost half the height to width aspect ratio or second shape factor, S_2 , of the NRB. The geometric

properties and theoretical buckling load, P_{crit} at 100% shear strain of the NRB and LRB can be found in Table 2-2. The theoretical bearing buckling loads presented are based on the overlapped area method of buckling calculations by Buckle and Liu (1993). To link the bearing properties to its supporting substructure, the columns are presented in terms of a stiffness ratio (SR) between the horizontal stiffness of the bearing and the column. With flexible column substructures, the stiffness of the column in the bearing-column subassembly is similar to a cantilever (Crowder and Becker, 2017). As a result, the SR for an elastomeric bearing supported by a column can be presented as

$$SR = \frac{K_{bearing}}{K_{column}} = \frac{\frac{GA}{t_r}}{\frac{3EI}{L^3}} \quad \text{Equation 2-1}$$

where G is the shear modulus of rubber, A is the area of rubber including cover, and t_r is sum of the thickness of rubber layers, while E , I , and L are the young's modulus, second moment of area, and length, respectively, of the supporting column. It should be noted that for the LRB, the SR presented is based on the theoretical secant stiffness of the LRB at 100% shear strain.

Table 2-1: Column properties

Column Type	Depth-to- Length (%)	I (10^6 mm^4)	SR_{NRB} (%)	SR_{LRB} (%)
HSS127x127x8.0	14.5	7.7	2.9	3.8
HSS102x102x8.0	11.6	3.7	6.1	7.8
HSS76x76x4.8	8.7	1.0	22.7	29.1

The NRB and LRB specimens were first tested under pure cyclic rotation with no displacement to establish a baseline rotational stiffness and then cyclic horizontal displacement with proportional rotation at the top of the bearing. A summary of the testing

schedule can be found in Appendix B. All tests were conducted at a velocity of 1 mm/s. All cyclic tests were performed at two different axial loads for each bearing. For the NRB, axial loads of 50 and 100 kN corresponding to 2.5 MPa and 5 MPa were used. For the LRB, axial loads of 50 kN and 80 kN corresponding to 1.25 MPa and 2 MPa were selected. The axial loads for the LRB were relatively small compared to typical design because of the low shape factor of the bearing, which results in low buckling loads.

Table 2-2: Bearing properties

Bearing Property	Natural Rubber Bearing (NRB)	Lead Rubber Bearing (LRB)
Radius, r (mm)	80.0	114.3
Area of rubber, A (mm ²)	20110.0	39900.0
Lead core radius (mm)	n/a	19.0
Rubber layer thickness, t (mm)	1.98	6.0
Steel shim thickness, t_s (mm)	1.0	2.7
Total rubber thickness, t_r (mm)	39.6	96.0
Height, h (mm)	101.8	210.0
Shape Factor, S_1	19.6	7.9
Shape Factor, S_2	4.5	2.4
Shear modulus, G (MPa)	0.4	0.4
Theoretical P_{crit} , 100% strain (kN)	475.4	102.6

Cyclic rotation tests used the 127x127x8.0 column (stiffest subassembly) to limit rotation at the base. Tests up to a peak of 0.02 rad were conducted for the NRB, while only tests up to 0.01 rad were conducted for the LRB. Top-plate rotational demands were limited to 0.01 rad for the LRB because of its low theoretical buckling load capacity and the decrease in buckling load with rotational flexibility. The applied rotation values were based on rotations observed by Crowder and Becker (2017), where 0.01 rad for the stiffest column specimen (SR = 2.9%) and 0.02 rad for the second stiffest column (SR = 6.1%) were

observed. These values are similar to those explored by other researchers (Karbakhsh Ravari et al., 2012, Ishii et al., 2017).

After establishing baseline rotational stiffnesses, the column-bearing assembly was tested quasi-statically, cycling the displacement at the base of the column and the rotation at the top of the bearing while maintaining constant axial load, similar to Crowder and Becker (2017). Cycles gradually increased up to 100 mm (253% shear strain for the NRB and 104% shear strain for the LRB) with two cycles at each displacement increment to scrag the bearing, as shown in Figure 2-4a. Rotations were increased proportionally to the displacement, as would be seen under typical first mode behaviour (see Figure 1-2) or from overturning moment, as seen experimentally in Chen et al. (2016). It should also be noted that for the 1.25 MPA axial load level, the LRB was tested to 80% shear strain due to system limitations. The deflected shape of the bearing during testing, as well as its positive force and displacement notation can be found in Figure 2-4b.

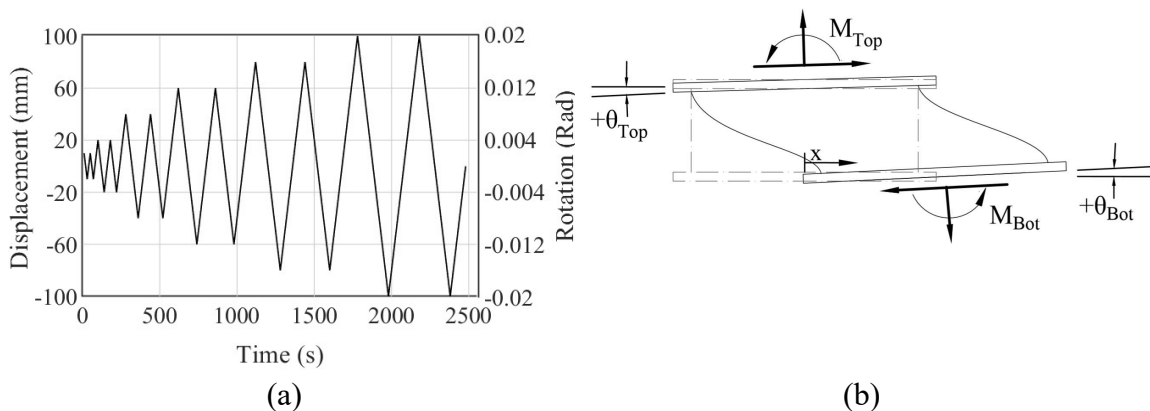


Figure 2-4: (a) Displacement protocol (b) Bearing positive notation

The NRB was then tested with the HSS127x127x8.0 and HSS102x102x8.0 columns monotonically to large shear strains (300%) under increasing axial load and checked for damage. Shear strains were limited to 300% as shear failure often occurs past 300% strain (Sanchez et al., 2013). The maximum axial load was limited by the experimental setup limitations. Axial loads were increased from 20% to 32% of the undeformed theoretical P_{crit} , or from 96% to 152% of the buckling load at 300% strain. The test axial loads compared to the Buckle and Liu (1993) overlapped area critical load reduction accounting for the Warn et al. (2007) extension of minimum vertical stiffness is shown in Figure 2-5. These theoretical buckling loads have been shown to be overly conservative in various experimental tests (Buckle et al., 2002, Cardone and Perrone, 2012, Sanchez et al., 2013); however, all previous stability testing was conducted with rigid boundary conditions. This has not been investigated with column-supported bearings.

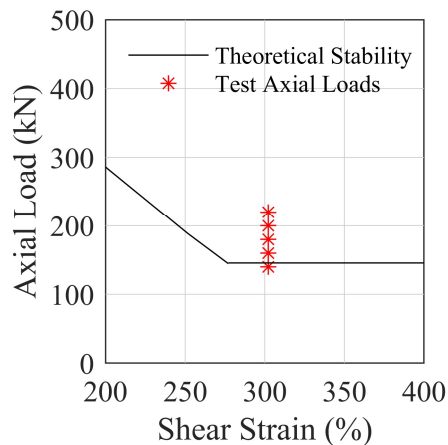


Figure 2-5: Comparison of theoretical buckling loads to testing protocol shown between 200 and 400% shear strain

2.1 Response of the Natural Rubber Bearing (NRB) Assemblies

2.1.1 Pure Rotation

The stiffest bearing-column subassembly, with the 127x127x8.0 column, was subjected to cyclic rotation of the top plate up to 0.02 rad, shown in Figure 2-6. Lateral displacement was minimal (<5 mm) but not zero due to the testing geometry. The results of the moment-rotation test applied at the top of the bearing is shown in Figure 2-7. While this loading condition is not pure bending, the moment-rotation is compared against the theoretical bending stiffness, based on incompressible rubber assumptions:

$$EI_{eff} = 2GIS_1^2 \quad \text{Equation 2-2}$$

where S_1 is the aspect ratio of a single layer of rubber. The theoretical bending stiffness captures the rotational behaviour of the bearing under typical rotations. With rotations larger than roughly 0.007 rad, the moment rotation relationship becomes nonlinear and the theoretical relationship no longer holds. The softening tangent stiffness increases with increased compressive load, which was also seen in Ishii et al. (2017), due to reduced tensile strains in the rubber.



Figure 2-6: Pure rotation test at +0.02 rad of top rotation

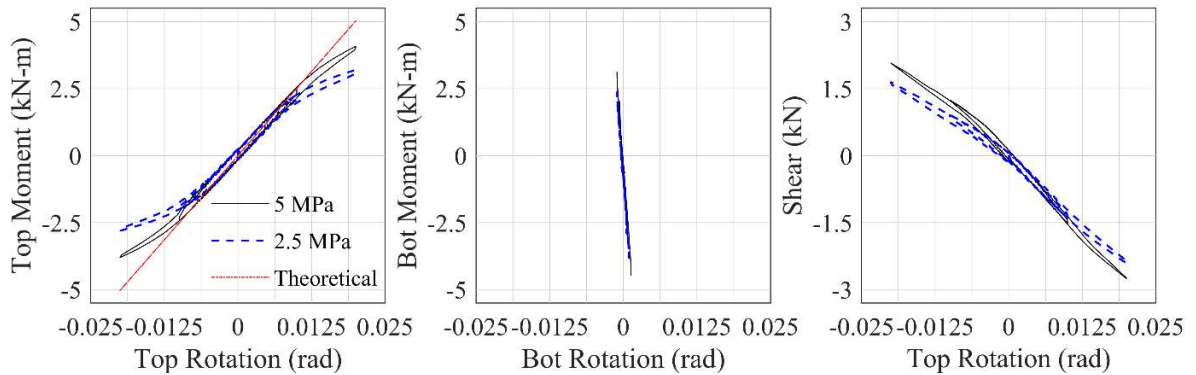


Figure 2-7: Bearing top moment-rotation (Left), bottom moment-rotation (Centre), and shear-rotation (Right) curves for the NRB pure rotation test under two axial load cases

2.1.2 Cyclic shear and rotation

The NRB was tested cyclically in a column-top assembly under 5 MPa (100kN) and 2.5 MPa (50kN) axial pressure with applied top rotations of 0 rad (rigid top), 0.01 rad, and 0.02 rad. The shear-displacement measured in the global horizontal axis and the top and bottom moment-rotation responses of the bearing with the three column assemblies under the range of applied top rotations with 5 MPa axial pressure are shown in Figure 2-8.

The global horizontal stiffness of the bearing is impacted by the presence of both top and bottom boundary rotation, θ_{top} and θ_{bot} . The rotation of the top plate of the bearing plate relative to the bearing plate is termed the local rotation, defined as

$$\theta_{local} = \theta_{top} - \theta_{bot} \quad \text{Equation 2-3}$$

While using θ_{local} to investigate bearing behaviour is most intuitive, there is a strong relationship with the total rotation of the bearing, θ_{total} , which is the total rotation applied to the end bearing boundaries shown as

$$\theta_{total} = \theta_{top} + \theta_{bot}$$

Equation 2-4

If both the top and the bottom of the bearing are rotated 0.02 rad clockwise, θ_{local} is 0 rad while θ_{total} is 0.04 rad. This scenario can be seen in Figure 2-9(b), where the top plate and bottom plate are equally rotated and represent a parallel, although flexible end condition.

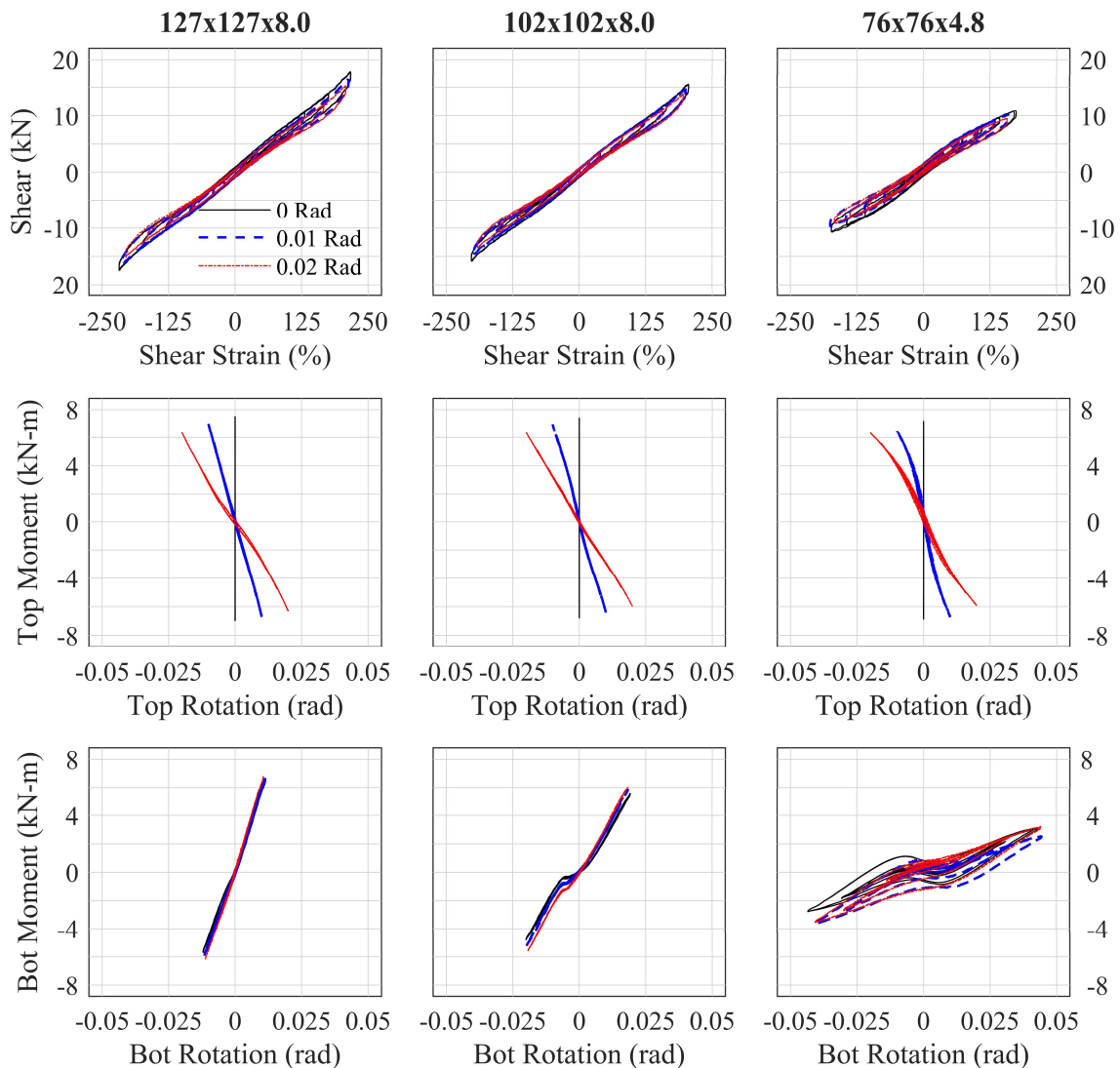


Figure 2-8: Shear-Shear strain, top and bottom moment-rotation responses of column subassemblies at 5 MPa axial load (100 kN)

Of note is the large rotation at the bearing-column interface seen in Figure 2-9, where the peak bottom plate rotations for the 127x127x8.0, 102x102x8.0, and 76x76x4.8 columns reached 0.012, 0.02, and 0.045 rad of rotation under rigid top conditions, respectively. Despite the largest column being horizontally stiff when compared to the NRB (SR = 2.9%), the magnitude of rotation at the column-bearing interface is much larger than in typical installations of bearings in buildings. For example, Chen et al. (2016) measured peak rotations of 0.00035 rad in a shake table test of a full-scale base-isolated building with rigid diaphragms.

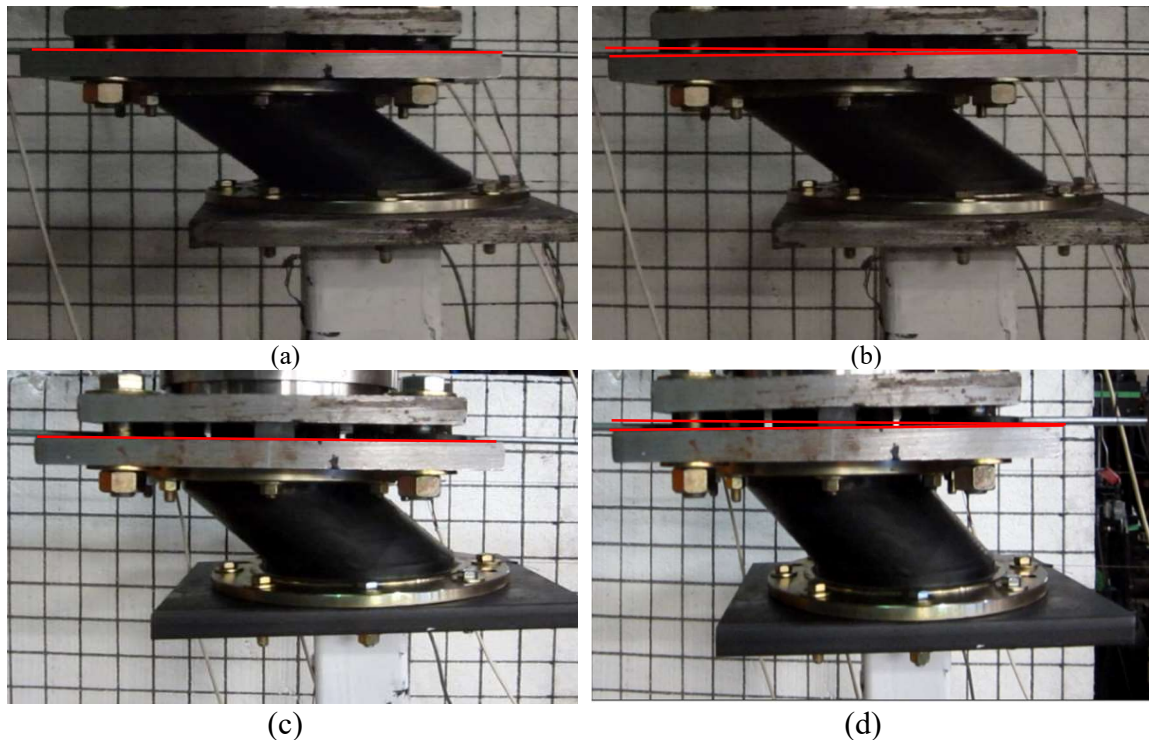


Figure 2-9: (a) NRB-102x102x8.0 with $\theta_{top} = 0$ (b) NRB-102x102x8.0 with $\theta_{top} = 0.02$ rotation, (c) NRB-76x76x4.8 with $\theta_{top} = 0$, (d) NRB-76x76x4.8 with $\theta_{top} = 0.02$

The horizontal stiffnesses are compared in Table 2-3, where the bearing secant stiffness at 100% shear strain at both load levels and peak θ_{top} and θ_{bot} are provided. The

combination of applied rotation and flexible supporting column can result in cumulative decreases in horizontal bearing stiffness of roughly 20%, but this scenario represents an extreme boundary case with a yielded column with a SR of 22.7% (peak $\theta_{bot} = 0.045$ rad) and an applied θ_{top} of 0.02 rad.

Table 2-3: Global NRB secant stiffness comparisons at 100% shear strain under varied boundary rotations and axial loading.

Supporting column	Peak Rotations (rad)			Bearing Secant Stiffnesses (N/mm)		Percent change compared to 127x127x8.0, 0 top rotation		Percent change compared to supporting column, 0 top rotation	
	θ_{top}	θ_{bot} 5 MPa	θ_{bot} 2.5MPa	5 MPa	2.5 MPa	5 MPa	2.5 MPa	5 MPa	2.5 MPa
127 x127 x8.0	0	0.012	0.013	214.1	214.7	/	/	/	/
	0.01	0.012	0.012	205.1	210.0	-4.2	-2.2	-4.2	-2.2
	0.02	0.012	0.012	196.7	204.7	-8.6	-4.6	-8.6	-4.6
102 x102 x8.0	0	0.020	0.020	204.0	218.0	-4.7	+1.6	/	/
	0.01	0.020	0.020	196.9	215.3	-8.0	+0.3	-3.5	-1.3
	0.02	0.019	0.019	187.9	205.6	-12.2	-4.2	-7.9	-5.7
76 x76 x4.8	0	0.045	0.040	186.3	201.3	-13.0	-6.3	/	/
	0.01	0.045	0.040	175.9	196.4	-17.9	-8.5	-5.6	-2.4
	0.02	0.045	0.040	171.6	188.4	-19.8	-12.2	-7.9	-6.4

The more realistic design scenarios are the 127x127x8.0 and 102x102x8.0 columns, where decreases in horizontal stiffness of roughly 4% to 13% were observed during the cyclic tests. The reduction in horizontal stiffness due to rotation is roughly 3.5-4.5% per 0.01 rad θ_{total} for 5 MPa and 1.5-2.5% per 0.01 rad θ_{total} for the 2.5 MPa load case, as shown in Figure 2-10. So, interestingly, the decrease in horizontal stiffness is approximately equal between tests when the θ_{total} is equal, regardless of at which end the rotation is applied. This

means that bearing test setups capable of rotating only one end plate can capture the expected decrease in horizontal stiffness by applying the θ_{total} instead of the predicted combination of θ_{top} and θ_{bot} .

The global horizontal stiffness is relevant to the design of the bearing and substructure in column top systems but bearing element models are also concerned with capturing the local shear behaviour. The effect of θ_{local} is explored on the local shear stiffness in Table 2-4, where the local shear stiffness is based on the horizontal force measured along the local axis of the bearing's rotated top plate.

Table 2-4: Local bearing secant stiffness comparisons at 100% shear strain under 5 MPa

Supporting column	Peak Rotations (rad)		Percent change compared to 127x127x8.0, $\theta_{top} = 0$ rad		Percent change compared to supporting column, $\theta_{top} = 0$ rad	
	θ_{top}	θ_{local}	Local 5 MPa	Local 2.5 MPa	Local 5 MPa	Local 2.5 MPa
127x127x8.0	0	-0.012	/	/	/	/
	0.01	-.002	+2.8	+0.7	+2.8	+0.7
	0.02	0.008	+3.5	+0.4	+3.5	+0.4
102x102x8.0	0	-0.020	-2.7	+0.5	/	/
	0.01	-0.010	-0.1	+2.5	+2.8	+2.1
	0.02	0	+2.5	+2.4	+5.4	+2.0
76x76x4.8	0	-0.045	-10.8	-4.7	/	/
	0.01	-0.035	-10.3	-2.5	+0.5	+2.3
	0.02	-0.025	-6.1	-1.7	+5.3	+3.1

The application of top rotation, θ_{top} , resulted in slightly increased local stiffness values. The increase in local shear stiffness compared to the rigid top case of the supporting column for applied top rotations up to 0.02 rad were up to 5.5%. In the case of the HSS127x127x8.0 with $\theta_{top} = 0.02$ rad, it is expected to see a decrease in stiffness at the when compared

because $\theta_{\text{local}} = +0.01$ rad. This was not seen for the 5 MPa load case, but there was a small decrease in the 2.5 MPa case compared to the $\theta_{\text{local}} = 0$ rad case (+0.7% to 0.4%).

Change of horizontal stiffness with pressure is well recognized as a combination of change in shear modulus of the elastomer, G (Stanton et al., 1990), and P- Δ effects (Koh & Kelly, 1988). However, here, even the coupling term with rotation is influenced. As seen in the different plots of Figure 2-10, larger axial load level pressure results in a higher decrease dependency of horizontal stiffness on rotation. This trend is more easily seen in Figure 2-11, which includes larger axial load levels from Section 3.3, where the more flexible columns have larger bearing stiffness decreases for the same axial load level. For example, the decrease in bearing stiffness at 100% shear strain with 0 rad of top rotation from the 127x127x8.0 column to 76x76x4.8 is 13% for the 5 MPa case but only 6.3% for the 2.5 MPa case.

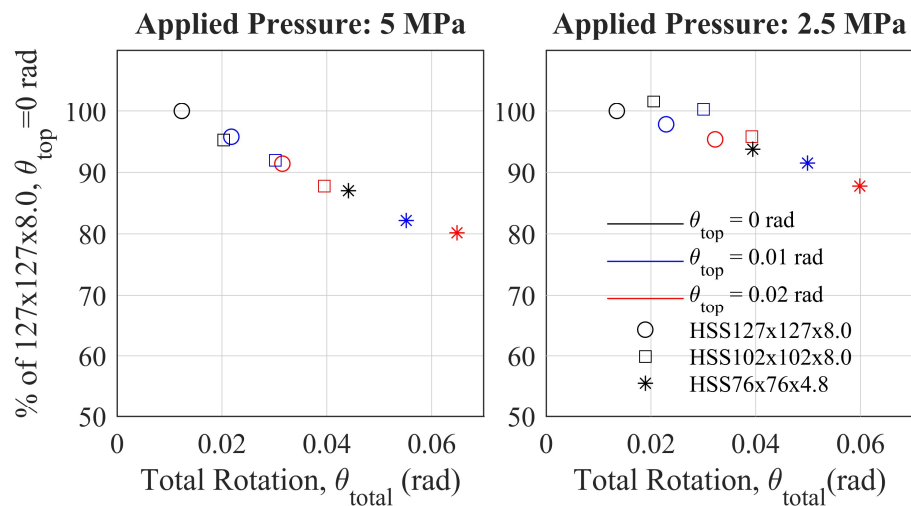


Figure 2-10: Bearing stiffness decrease with total rotation, θ_{total} , at 100% shear strain and (a) 5 MPa and (b) 2.5 MPa compared against HSS127x127x8.0 with rigid top conditions

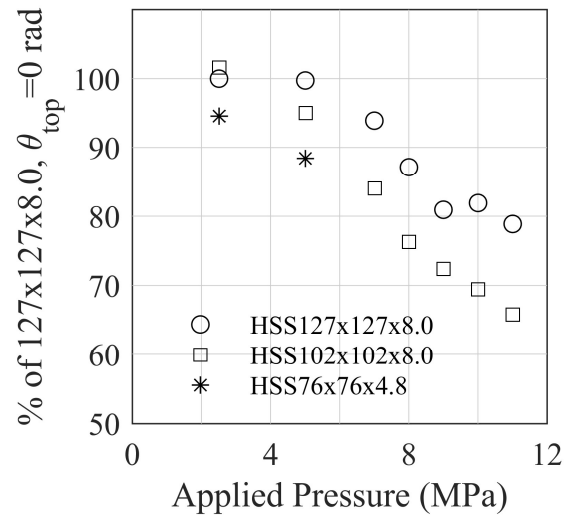


Figure 2-11: Bearing stiffness decrease with axial pressure at 100% shear strain and $\theta_{top} = 0$ rad, compared against HSS127x127x8.0 with rigid top conditions at 2.5 MPa

This trend agrees with the conclusion drawn by Karbaksh Ravari et al. (2012) from the Haringx (1949) derivation for rotated boundary conditions, where the horizontal stiffness decrease due to rotated boundary conditions is a function of axial loading. This may be relevant when considering torsion in a column-top isolated structure where external and corner columns often support lower loads than interior columns.

The effects of rotation and axial load on horizontal stiffness have been explored at a shear strain of 100%. A comparison of secant stiffnesses with different end conditions at all shear strains is shown in Figure 2-12. The theoretical stiffness, the numerator of Equation 2-1, is shown with a horizontal line and is based on a constant shear modulus, G . Applied top rotation θ_{top} shifts the stiffness down, but does not change the rate of stiffness decrease with increasing strain and bottom rotation. Thus, the findings from the previous paragraphs are relevant across the horizontal shear strains measured.

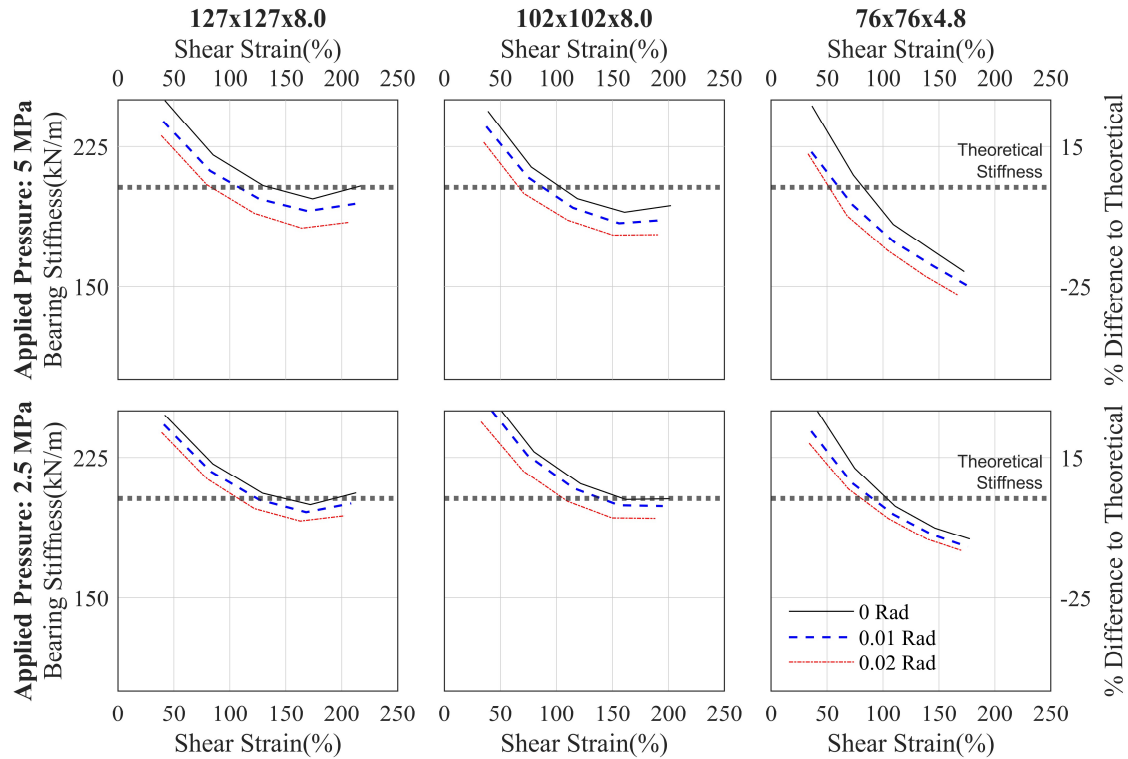


Figure 2-12: Comparison of global NRB stiffnesses at varied loads and applied top-plate rotation

Furthermore, the theoretical stiffness overpredicts the bearing stiffness at large shear strains with axial load and rotation. For the extreme boundary case of the 76x76x4.8 column with $\theta_{top} = 0.02$ rad, the theoretical stiffness overestimates the bearing stiffness by up to 25%. This is relevant to the design of a column-top system as lower bearing stiffness will result in higher displacements, which will lead to greater P- Δ forces on the column subassemblies.

One of the goals of the model proposed by Ishii et al. (2017) was to capture the asymmetrically distributed bending moments caused by flexible boundary conditions. The outcomes of asymmetric bending moment distributions with flexible supporting structures were noted by Crowder and Becker (2017) where rotation of the column-bearing interface shifted the point of inflection towards the column and in some cases, into the column, which

results in single curvature of the bearing. This behaviour was observed for the 76x76x4.8 column for the rigid top case, and the resulting moment-rotation behaviour (shown in the bottom moment-rotation plot of Figure 2-8) is cubic. This behaviour was not observed with the same column subassembly when top rotation was applied as the point of inflection shifted back up with θ_{top} . In the top moment-rotation plots of Figure 2-8, there is a small decrease in top bearing moment per rad of applied rotation as the boundary condition transitions from a fixed-rotation end to more of a rotational spring. The decrease in moment at the top of the bearing due to the added rotation was only 29% of the moment found from the pure rotation test (Figure 2-7), confirming that the rotational stiffness significantly decreased with shear strain, as seen in Ishii et al. (2017).

Both the bottom moment and rotation were influenced by the application of rotation at the top of the bearing. While the rotation at the top increased the bottom moment, it also decreased the bottom rotation by up to 10%. Thus, while the decreased horizontal stiffness is dependent on θ_{total} , the distribution of bending moment is dependent on the rotation of one plate with respect to the other θ_{local} . This can be seen in the top moment-rotation plot of Figure 2-8 when the rotation is equal at the top and bottom plate, such as for the 102x102x8.0 column with 0.02 rad of applied rotation. In these essentially parallel boundary conditions, the top and bottom have nearly equal moments. Furthermore, when there is a difference between θ_{top} and θ_{bot} , there is a nonlinear moment-rotation relationship with curvature that changes with the magnitude of θ_{top} relative to θ_{bot} . This moment-rotation relationship is linear when parallel boundary conditions are maintained ($\theta_{local} = 0$ rad).

2.1.3 Larger strain testing

In order to test to larger strains, the setup was altered to maintain rigid top plate conditions and to allow for one-sided displacements up to 200mm. The NRB was tested to 300% shear strain under axial loads of 7 to 11 MPa. These axial loads correspond to 96% to 150% of the theoretical overlap buckling load with parallel endplates at 300% shear strain, which can be found in Figure 2-5. The deformed shape at 300% shear strain is shown in Figure 2-13.

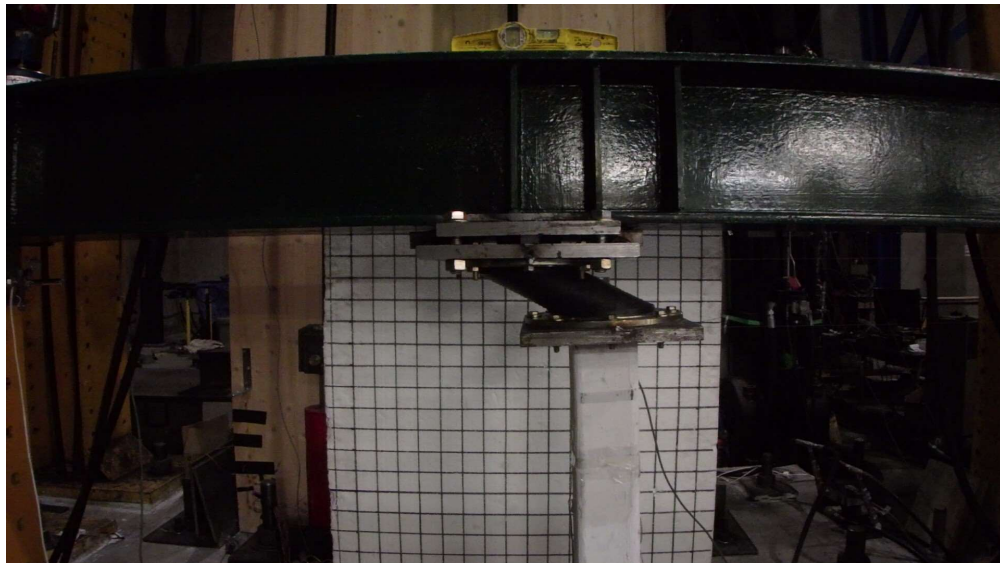


Figure 2-13: NRB tested to 300% shear strain supported by the 102x102x8.0

The shear- shear strain plots and bearing moment-rotation plots are presented in Figure 2-14. The theoretical stiffness presented is the linear approximation based on a constant shear modulus. Both columns experienced minor inelastic yielding, as can be seen in the bearing moment-rotation plots at 7 MPa (the first test) where the plot shows residual rotation. Despite minor yielding of the column and testing up to 150% the theoretical buckling load, none of the bearing-column subassemblies exhibited negative stiffness.

Thus, the simplified overlap method can still be used when the bearings are mounted on flexible supports designed to stay elastic. This finding is limited to bearings of similar shape factor as bearings with lower shape factors are more susceptible to instability.

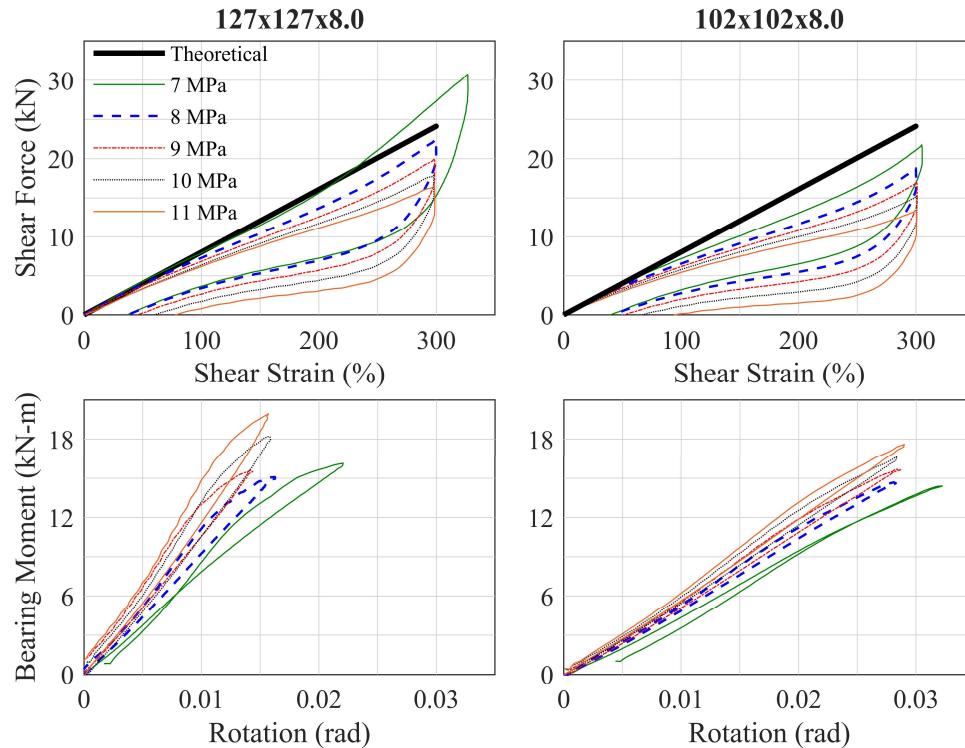


Figure 2-14: Monotonic shear-strain and bottom bearing moment-rotation curves for 127x127x8.0 (left) and 102x102x8.0 (right) subassemblies

Table 2-5 compares the secant stiffnesses at 300% shear strain at each load level. With both columns, which are relatively stiff with SRs of less than 10%, the horizontal stiffness was reduced by 16-23%. As these reductions are relative to the HSS127x127x8.0 (SR = 2.9%) case, which cannot be considered a rigid boundary as it experienced 0.016 rad of rotation at the bearing-column interface, the loss in stiffness due to flexible boundaries

is even higher when compared to rigid diaphragm boundary conditions. The trend in decrease of horizontal stiffness per rad of rotation was found to be roughly 4% at an axial load level of 5 MPa in Section 3.2. The decrease per rad in horizontal stiffness between the two columns tested to 300% shear strain was higher than predicted before, as shown in Table 2-5, where the decrease per rad of rotation was found to be between 11.3 and 17.3%. This is different than the decreases in secant stiffness taken at 100% shear strain, shown in Table 2-6, where the decrease in stiffness generally followed the trends from Section 3.2.

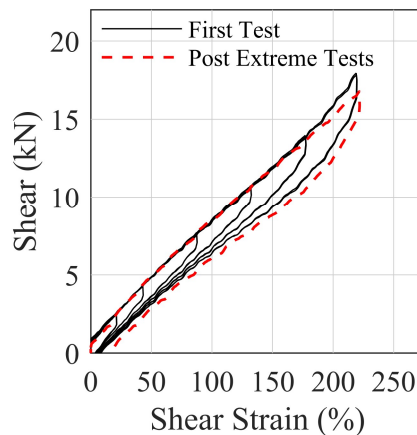
Table 2-5: Secant stiffnesses (N/mm) at 300% shear strain at varied load levels

Supporting Column	7 MPa	8 MPa	9 MPa	10 MPa	11 MPa	% Δ 11 to 7 MPa
HSS127x127x8.0	228.6	188.1	168.5	156.0	144.2	-36.9
HSS102x102x8.0	177.0	156.7	141.2	126.3	111.5	-37.0
% change due to column flexibility	-22.6	-16.7	-16.2	-19.0	-22.7	
% decrease per rad of peak θ_{bot}	17.3	13.9	11.3	15.1	17.1	

Table 2-6: Secant stiffnesses (N/mm) at 100% shear strain at varied load levels

Supporting Column	7 MPa	8 MPa	9 MPa	10 MPa	11 MPa	% Δ 11 to 7 MPa
HSS127x127x8.0	201.6	187.0	173.7	175.8	169.3	-16.0
HSS102x102x8.0	180.4	163.8	155.3	149.0	141.2	-21.7
% change due to column flexibility	-10.5	-12.4	-10.6	-15.2	-16.5	
% decrease per rad of peak θ_{bot}	5.9	7.0	5.6	9.0	9.7	

The maximum axial pressure used for the 300% shear strain tests was 11 MPa which resulted in 0.016 rad and 0.029 rad of rotation at the bottom of the bearing for the 127x127x8.0 and 102x102x8.0 subassemblies, respectively. The bearing was then tested to 200% strain under 5 MPa to compare against the original behaviour. The comparison is shown in Figure 2-15. The one-sided hysteresis loop is nearly identical to that from before large rotations were imposed; however, there is no longer strain hardening at 200% shear strain. This shows excellent bearing resiliency combined shear strain and large rotation.

**Figure 2-15:** Behaviour pre and post extreme loading scenarios, 5 MPa

2.1.4 *Comparison with simplified models*

In some bearing models, the moment-rotation stiffness is taken as the theoretical stiffness at zero shear strain with no coupling off-diagonal terms. These models might utilize empirically derived equations to account for behaviours such as P- Δ effects. They are more computationally efficient while being sufficient for isolation with rotationally rigid boundary conditions. However, Ishii et al. (2017) showed that rotational stiffness is significantly reduced at large shear strains, which was further proven experimentally in Section 2.1.2. For applications that include boundary rotation and a model using linear, uncoupled rotation springs, it is perhaps more appropriate to use the reduced effective rotational stiffness based on a bearing's design displacement for stiffness matrix models with zero off-diagonal terms.

The experimental tests were modelled in OpenSees (McKenna & Fenvez, 2006) using two elastomeric bearing elements to assess how rotation effects are captured in currently available models, the ElastomericX bearing element (Kumar et al, 2015) and the Crowder and Becker (2017) linear model. The three-dimensional ElastomericX bearing element has options to include decrease in buckling loads for overlapping effects, variation in the shear stiffness with axial loads, and variation in vertical stiffness with horizontal displacement. The decrease in buckling loads for overlapping effects was not included as the experiment has already shown to exceed the theoretical buckling loads and including them would lead to premature negative stiffness. Omitting this tag, however, removes the majority of softening due to axial load. In terms of rotation, the drawback with this model for a column-top system is that it uses linear-elastic rotation springs with no off diagonal (coupling)

terms. The Crowder and Becker (2017) model is a two-dimensional stiffness matrix bearing element based on Haringx's theory (1949) and the analytical stiffness matrix model by Chang (2002). This model uses coupling terms for the rotational springs, relevant to column-top isolation systems, as the impact of rotation on horizontal stiffness is accounted for. The columns were modelled as displacement-based beam columns with constructed fiber sections using the stress-strain behaviour of the Giuffrè-Menegotto-Pinto hysteretic model.

Three cases, all with 5 MPa (100 kN), were compared. The first case is when the bottom rotation is larger than the top rotation, i.e. the most flexible column with zero rotation at the top. The second case is when the bottom rotation is roughly equal to the top rotation, i.e. the 102x102x8.0 column with 0.02 rad peak top rotation, and the last case is when the top rotation is greater than the bottom rotation, i.e. the 127x127x8.0 column with 0.02 rad applied rotation. This corresponds to $\theta_{\text{total}} = 0.032, 0.04, \text{ and } 0.045$ respectively and $\theta_{\text{local}} = 0.008 \text{ rad}, 0.001 \text{ rad}, \text{ and } -0.045 \text{ rad}$. The shear-shear strain, top moment-rotation and bottom moment-rotation results of the numerical simulations are shown in Figure 2-16.

The rotation-displacement coupled model of Crowder and Becker (2017) captures the effective stiffness of the 127x127x8.0 and 102x102x8.0 subassemblies at the peak experimental displacement within 1.5% error while the uncoupled model of Kumar et al. (2015) captures the effective stiffness within 12.5%. This aligns with the previous conclusions, as boundary rotation accounted for a 5-15% decrease in horizontal stiffness. For the 76x76x4.8 subassembly, the Crowder and Becker (2017) model captured the

stiffness within 10% and the Kumar et al. (2015) model captures the stiffness within 25% error.

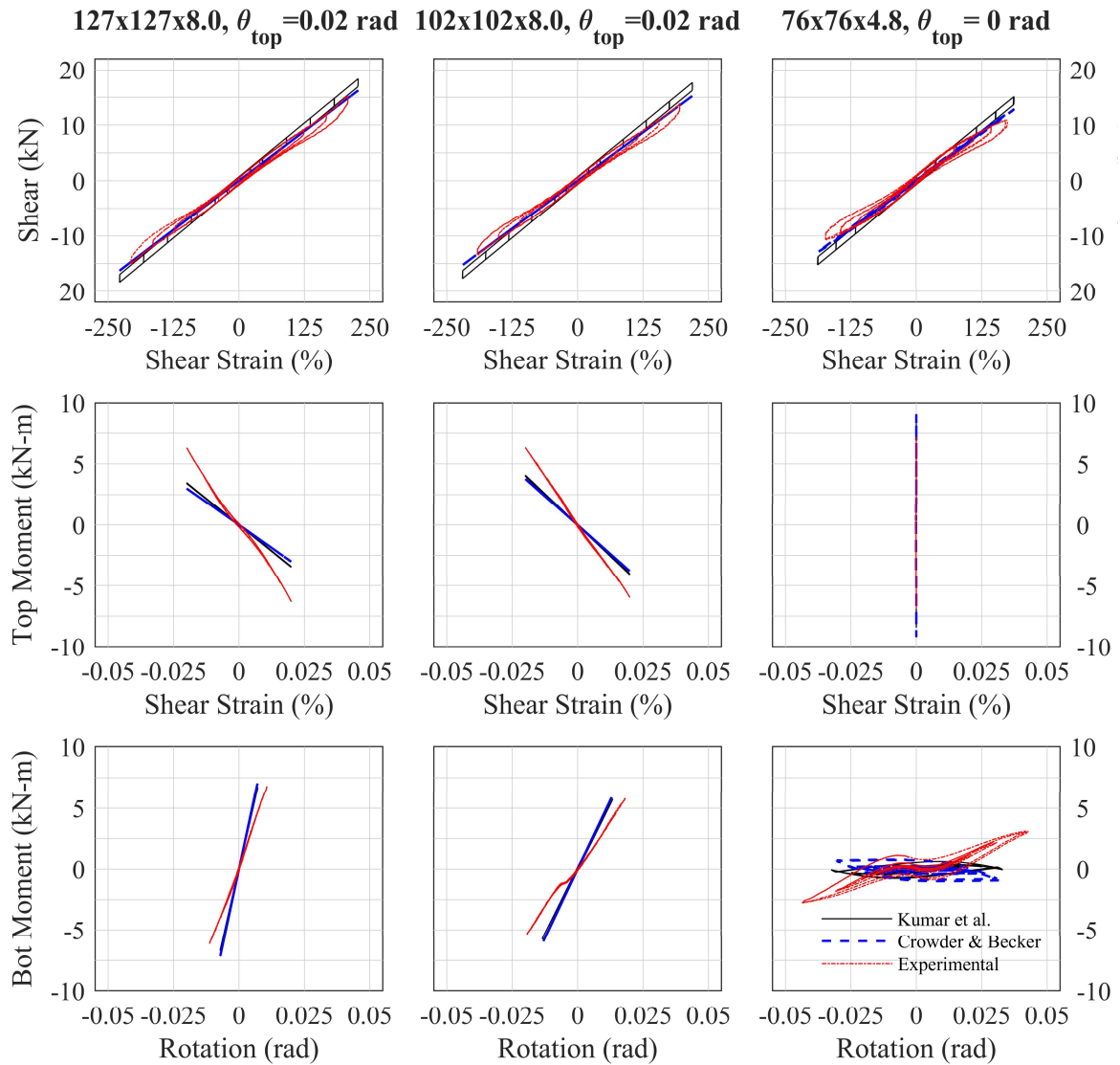


Figure 2-16: Force-displacement, top and bottom moment-rotation responses of the modelled vs experimental column subassemblies at 5 MPa axial load (100 kN)

Both models underestimated the rotation at the column-bearing interface. This can especially be seen with the 76x76x4.8 column, where the models underestimate the

interface rotation by up to 30%. This is because the rotational stiffness for both models use a linear rotational stiffness from pure rotation tests, which is a poor assumption when a bearing is subject to shear strain.

He et al. (2012) proposed a non-linear rotational stiffness equation to account for the dramatic decrease in rotational stiffness with shear strain. It is simple to use as it considers only shear strain, ignoring effects of axial loading of experimentally derived angles where the moment-rotation behaviour transitions from linear to non-linear. It is presented as

$$K_{rm} = K_{rm0} \left(1 - \left| \frac{\Delta}{D} \right|^{\frac{1}{1+\gamma^2}} \right) \quad \text{Equation 2-5}$$

where K_{rm} is the rotational stiffness at the bearing shear strain, γ , K_{rm0} is the rotational stiffness at zero shear strain, Δ is the displacement, and D is the bearing diameter. This equation is compared against the moment due to the applied rotation in Figure 2-17, obtained by subtracting the top-bearing moment from the tests with 0.02 rad of applied rotation from the top-bearing moment from the tests with a rigid top boundary. The theoretical rotational stiffness equation sufficiently captures the moment-rotation behaviour for all three column subassemblies; however, since axial load is not a consideration in Equation 2-5, there are limitations to the accuracy. From the measured moment-rotation relationships in Figure 2-17, the theoretical equation better estimates the rotational stiffness for low axial loads, with stiff subassemblies (SR < 10%). This makes sense as it was concluded in Section 2.1.1 that higher axial load leads to higher tangential rotational stiffness in the non-linear range.

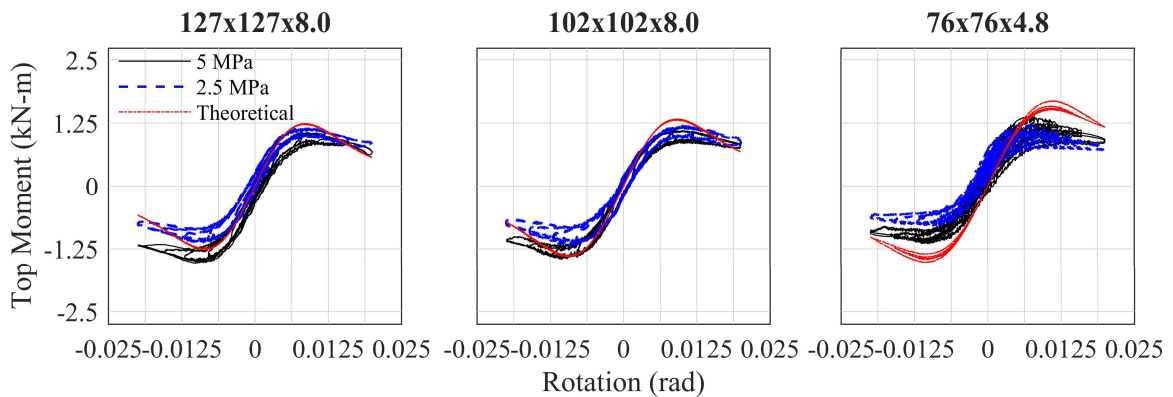


Figure 2-17: Comparison of Equation 2-5 with the NRB moment-rotation curves due to applied moment

The results of this equation can be easily incorporated into models by allowing for manual inputs of rotational stiffness, in lieu of automatically calculating the rotational stiffness based on geometric properties. The effective rotational stiffness would better approximate the moments transmitted by the isolators bounded by flexible framing.

2.2 Response of the Lead Rubber Bearing Assemblies

2.2.1 Pure rotation

Similar to the NRB, a rotation test was carried out on the LRB while supported by the HSS127x127x8.0. The top moment-rotation, bottom moment-rotation and shear-rotation plots are shown in Figure 2-18. The main difference for this test is that the LRB has a significantly lower shape factor than the NRB (S_I of 7.9 compared to 19.6), and thus, the rotational stiffness of the bearing is much lower. The moment-rotation is compared against the theoretical bending stiffness from Equation 2-2, where the stiffness coefficient is modified to account for the lead core and annular shape. To modify for annular rubber, the rotational stiffness coefficient is 2.5 instead of 2. (Kelly & Konstantinidis, 2011)

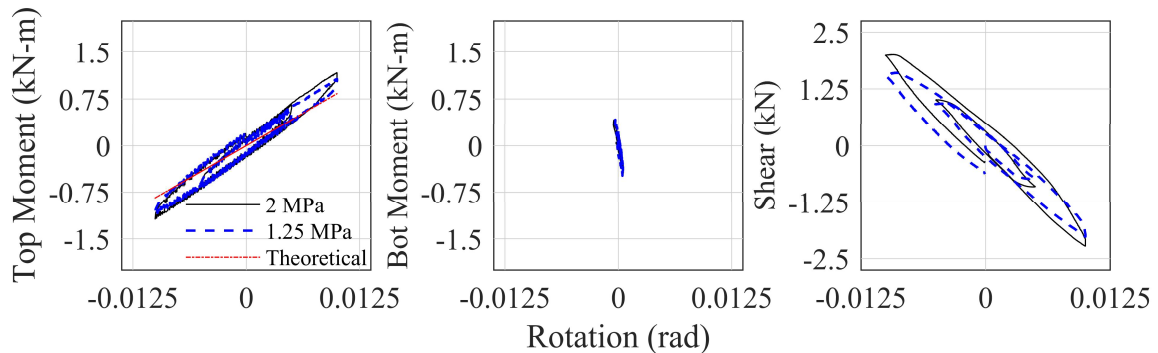


Figure 2-18: Bearing top moment-rotation (Left), bottom moment-rotation (Centre), and shear-rotation (Right) curves for the LRB pure rotation test under two axial load cases

The theoretical stiffness underestimates the rotational stiffness by almost 30%; however, for this bearing, the moment-rotation is linear up to the peak test rotation of 0.01 rad. This is in contrast to the NRB, where the pure moment-rotation plot was nonlinear after 0.007 rad. The bearing experienced minor lateral displacements (less than 3 mm) due to the testing geometry, but these minor displacements resulted in high shear forces due to the stiffness of the pre-yield lead core. The shear force from the lead core also leads to different magnitudes in the top and bottom moments, where the difference between the top and bottom moments is the measured shear at the top multiplied by the bearing height, for the pure rotation case.

2.2.2 Cyclic testing

The lead rubber bearing was tested cyclically in a column-top isolation assembly under two loading levels of 2 MPa (80 kN) and 1.25 MPa (50kN) with applied top rotations of 0 rad (rigid top) and 0.01 rad. These applied axial loads are comparatively lower than typical target design values due to the slender design of the bearing (S_2 of 2.38). The 1.25 MPa tests were only tested up to 80 mm (80% shear strain) instead of 100 mm (100% shear

strain) due to system limitations. The global shear-displacement and top and bottom moment-rotation responses of the bearing with the three column assemblies under the range of applied top rotations are shown in Figure 2-19.

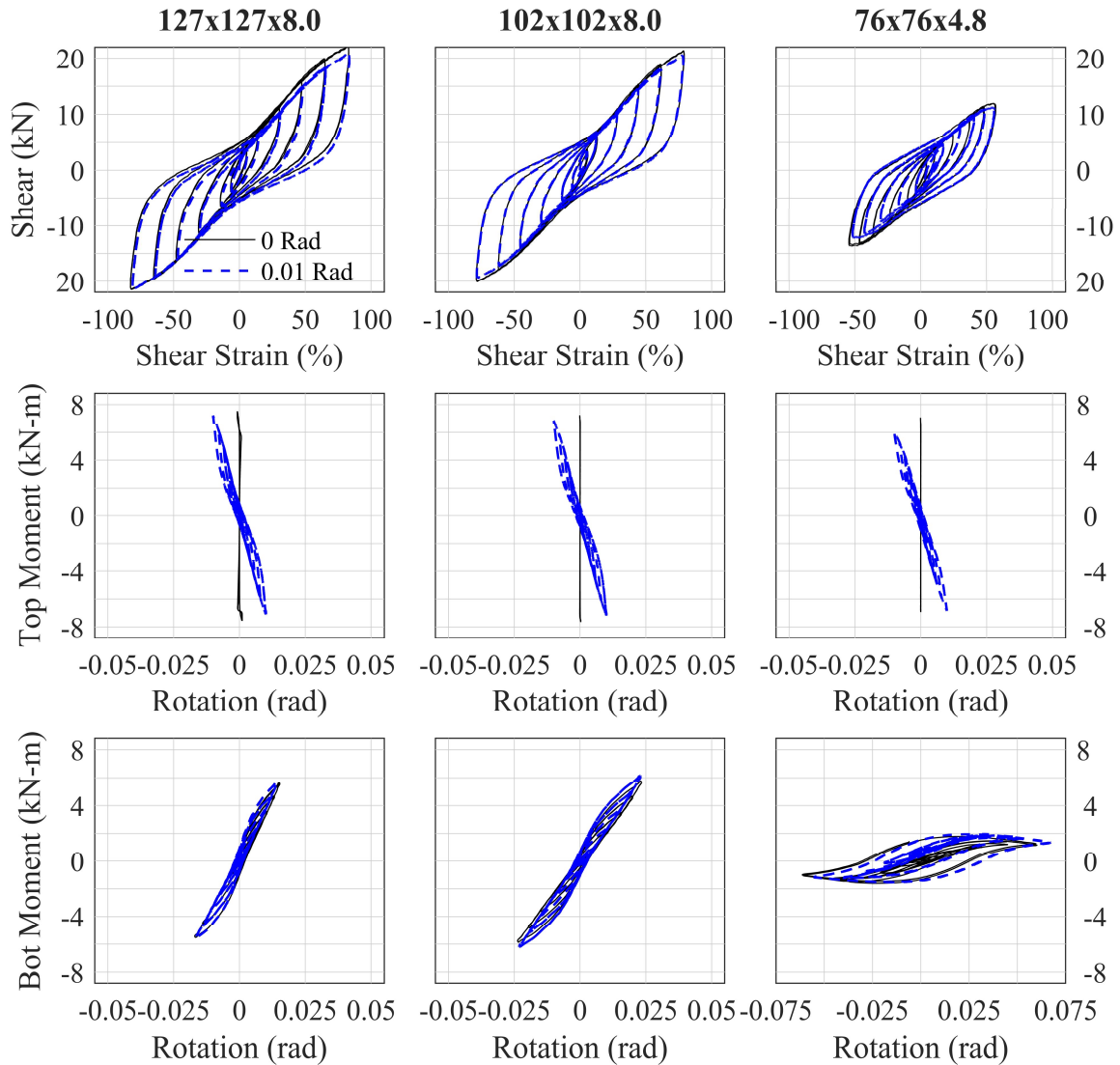


Figure 2-19: Shear-Shear strain, top and bottom moment-rotation responses of column subassemblies at 2 MPa axial load (80 kN)

An interesting behaviour found in the shear-displacement plot of the LRB is pinching in the LRB hysteresis for the 127x127x8.0 and 102x102x8.0 subassemblies. This behaviour

is not as pronounced in the hysteresis loop for the 76x76x8.0 subassembly because of the added hysteretic dissipation from the yielding column. This pinching behaviour is caused by a lack of confinement of the lead core due to light axial loads. The lead core cannot reach its full yield strength if lightly loaded due to vertical slippage of the sides of the lead core or horizontal slippage of the ends of the lead core (Skinner et al. 1993). A method to increase confinement of the lead core, other than increasing axial pressure, is decreasing rubber layer thickness (Ryan et al. 2005). As the S_I of the LRB is low (relatively large rubber layer thickness) and was lightly axially loaded, this effect was pronounced. This is relevant in a column-top system because corner and external columns are often lightly loaded. While this may be unavoidable in some design scenarios, the decrease in damping should be incorporated in analysis.

Similar to the NRB subassemblies, global horizontal stiffness decreases with application of top bearing rotation and with decreasing column size. Under rigid top conditions, the peak bottom plate rotations, θ_{bot} , for the 127x127x8.0, 102x102x8.0, and 76x76x4.8 columns reached 0.017, 0.024, and 0.065 rad of rotation respectively. The two more flexible column subassemblies are shown at max bearing shear strain with 2 MPa of axial pressure in Figure 2-20. While the shear strain demands and axial loads are relatively low, these are extreme rotational demands. The decreases in horizontal stiffness due to the large rotations are shown in Table 2-7 where the bearing secant stiffness is compared at 40% shear strain. The reduction in horizontal stiffness is very similar to the NRB, where a decrease of roughly 3.5-4.5% per 0.01 rad θ_{total} under both axial pressures was observed.

The axial pressure had a less significant impact than it did on the NRB, but this is likely because both are relatively small.

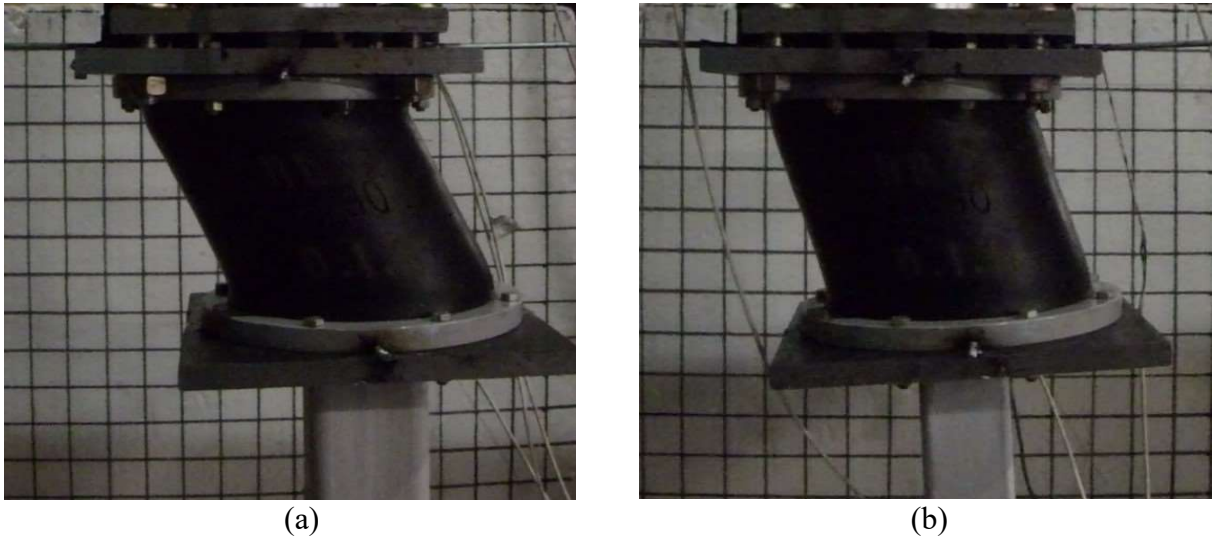


Figure 2-20: (a) NRB-102x102x8.0 with $\theta_{top} = 0$ rad (b) NRB-76x76x4.8 with $\theta_{top} = 0$ rad

Table 2-7: Global LRB specimen secant stiffness comparisons at 40% shear strain under varied boundary rotations and axial loading.

Supporting column	Peak Rotations (rad)			Percent change compared to 127x127x8.0, 0 top rotation		Percent change compared to supporting column, 0 top rotation	
	θ_{top}	θ_{bot} 2 MPa	θ_{bot} 1.25 MPa	2 MPa	1.25 MPa	2 MPa	1.25 MPa
127x127x8 .0	0	0.017	0.017	/	/	/	/
	0.01	0.017	0.016	-4.6	-4.2	-4.6	-4.2
102x102x8 .0	0	0.024	0.022	-3.8	-3.8	/	/
	0.01	0.024	0.021	-8.2	-8.5	-4.6	-4.9
76x76x4.8	0	0.065	0.053	-21.6	-14.7	/	/
	0.01	0.068	0.045	-27.6	-18.9	-7.5	-4.9

A comparison of the bearing secant stiffnesses with different end conditions is shown in Figure 2-21. The theoretical stiffness is calculated as

$$k_{eff} = Q_d + K_{rubber}\Delta$$

Equation 2-6

where Q_d is the characteristic strength of the bearing, controlled by the yield strength of the lead core, K_{rubber} is the horizontal stiffness of the rubber or the top term of Equation 2-1, and Δ is the displacement of the bearing.

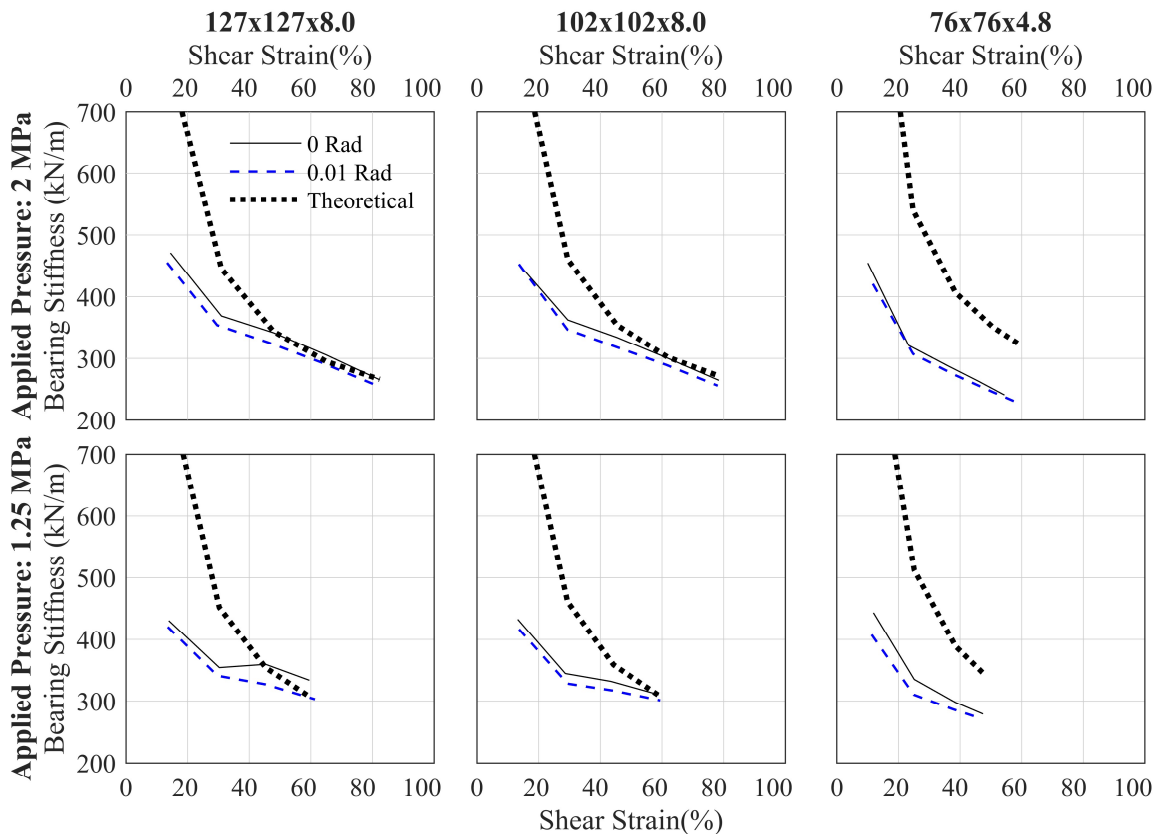


Figure 2-21: Comparison of LRB stiffnesses at varied pressures and applied top-plate rotation

At low shear strains, the theoretical stiffness highly overestimates the stiffness of the LRB because of the lightly loaded, unconfined lead core being unable to reach its full yield strength. For both the 127x127x8.0 and 102x102x8.0 columns, the theoretical secant stiffness aligns well with the secant stiffness after shear strains of roughly 50%, despite

experiencing bottom plate rotations of up to 0.025 rad under rigid top conditions. For the 76x76x4.8 column, which experienced significant yielding under the large rotations, the stiffness of the bearing is significantly lower than the theoretical prediction, which is unsurprising when taking into account a bearing-column interface rotation of 0.062 rad.

The 76x76x4.8 presents an extreme boundary condition, where the extreme yielding of the column and bottom rotation of the bearing caused near-buckling behaviour for the 2 MPa load case. This can be seen in the 76x76x4.8 force-displacement plot of Figure 2-20, where the tangent stiffness approaches zero. At this shear strain and load level (55% and 2 MPa respectively), the theoretical buckling load is roughly double (4.2 MPa or 170 kN). Thus, the flexible boundary conditions have a significant effect on the buckling loads for bearings with low shape factors ($S_1 < 10$, $S_2 < 2.5$). This contrasts against the NRB ($S_1 = 19.6$, $S_2 = 7.9$) conclusions, where the theoretical stiffness was conservative and can still be used as a design limitation.

In Section 2.1.4, Equation 2-5 proposed by He et al. (2012) was evaluated for the NRB, finding that the equation was able to sufficiently predict the rotational stiffness of the bearing when subject to shear strain, given its simplicity to use. To expand this conclusion, Equation 2-5 was also compared to the annular LRB with lower shape factors, seen in Figure 2-22. Similarly, the equation can sufficiently predict the change in rotational stiffness with shear strain, given its ease of use requiring only shear strain inputs. This conclusion is limited to lower axial loads, as from the pure rotation test, axial loading increases the tangential stiffness of the non-linear rotational stiffness.

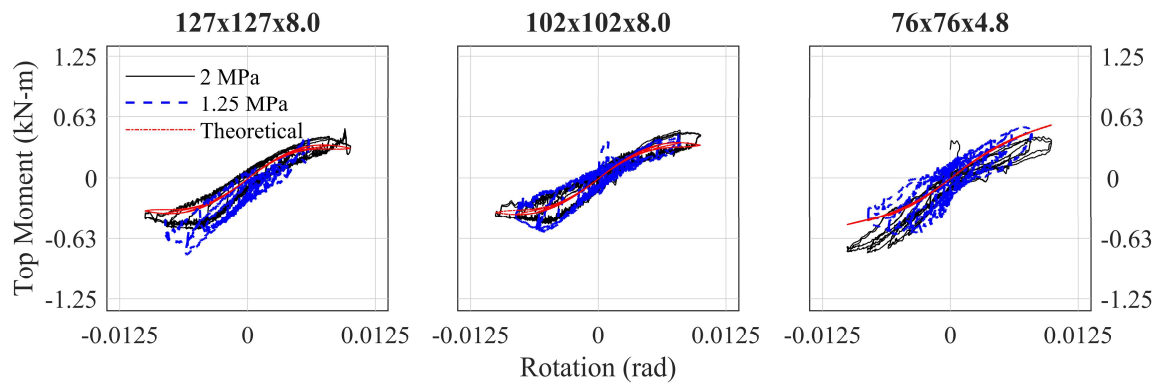


Figure 2-22: Comparison of Equation 2-5 with the LRB moment-rotation curves due to applied moment

3 CONCLUSIONS AND RECOMMENDATIONS

3.1 Conclusions

Traditional applications of isolation use rigid diaphragms to bound the end plates of bearings, resulting in very small to zero rotation. The design methodologies and analytical models commonly used to predict bearing behaviour are informed by experimental testing that is based on these rigid boundary conditions. When placing bearings on top of columns, the isolators are potentially bounded by flexible framing, allowing for rotation of the bearing end plates. Quarter-scale, quasi-static experimental testing was conducted to investigate the effects of rotation of both end plates on NRB and LRB behaviour. The results of the cyclic NRB tests were compared against OpenSEES simulations of currently available models. The following conclusions were made:

1. The horizontal stiffness of an elastomeric bearing decreases from a combination of both bottom and top plate rotation, regardless of the magnitude of rotation of one plate with respect to the other. If both plates are rotated equal amounts, representing a case where the bearing is in pure shear, the horizontal stiffness is decreased by the same amount as if one plate is unrotated and the other experiences twice the rotation. This means that test setups capable of only rotating one bearing end can capture the decrease in horizontal stiffness even if both ends can rotate.
2. The decrease in horizontal stiffness with rotation is a function of the axial load. A larger axial load will lead to a larger reduction in horizontal stiffness due to rotation. This is relevant in column-top isolation systems as external and corner columns are lightly loaded compared to internal columns.

3. Reasonable assumptions of stiffness degradation due to rotation would be 5-15% when the SR of the supporting column is under 10%. This was seen for both the NRB of $S_1 = 19.6$ and the LRB of $S_1 = 7.9$. Extreme scenarios (highly yielded support column, high axial loading) can see up to 30%.
4. Elastomeric bearings show excellent resiliency after significant loading. The NRB experienced a combination of rotation of 0.03 rad, 300% shear strain, and axial load 150% above the theoretical buckling load. The LRB was tested under a combination of rotation of 0.065 rad, 55% shear strain, and 47% of the overlap buckling load (2 MPa). Bearings that experience this level of loading do not need to be replaced unless significant visual damage is noticed, but this conclusion is limited to the rubber compound used and manufacturer.
5. Current models that do not consider coupling terms with rotation overestimate the horizontal stiffness of the bearing. Models with linear springs for rotational stiffness can underestimate the rotation at the column-bearing interface by up to 30% and do a poor job of modeling the distribution of the moments between the top and bottom plate.
6. The rotational stiffness significantly decreases with shear strain. The equation proposed by He et al. (2012), which describes the rotational stiffness in terms of shear strain, well captures the stiffness of both the NRB and LRB tested. Higher axial loads, which increase tangential non-linear rotational stiffness due to decreased rubber tensile loads with rotation, will lead to more inaccurate estimates using the equation.
7. For the bearing of $S_1 = 19.6$, the theoretical buckling equation still provides a conservative estimation of the critical capacity, even with minor column yielding. For

the LRB of $S_1 = 7.9$, under extreme rotation (seen as 0.065 rad) and yielding support column, the buckling load can be as little as half of the theoretical buckling load.

3.2 Recommendations for Future Work

To make column-top isolation a more attractive design option, further experimental and analytical work is recommended.

1. As with all quasi-static tests, there are limitations to the conclusions drawn if bearing behaviour changes significantly with strain rate. For LRBs, heating of the lead core can lead to considerable decrease in shear strength. While the damping is hysteretic and unaffected by strain rate, the temperature increase with dynamic loading can be significant. As a result, it is recommended that column-top systems are tested dynamically. This will provide information about the effect of lead core heating on rotational stiffness and combined rotational and temperature related effects on horizontal stiffness.
2. The axial load was held constant during the experiments but overturning effects can result in small axial loads or even tension on the bearings. Combined shear, tension, and rotation tests should be conducted to establish minimum load limits for column-top isolation systems. The tensile strains experienced with combined shear, rotation, and uplift could lead to cavitation or rupture of the rubber.

The results presented here are based on two separate shape factors and while conclusions can be generally made, there is insufficient information to establish trends based on shape factor. A more thorough experimental investigation of flexible conditions

on isolators of varied shape factors, controlling for all other variables, is recommended.

This is especially true for stability limits of isolators.

4 REFERENCES

- Commonwealth Historic Resource Management Limited. (2007). *Vancouver Schools: Establishing their Heritage Value*. Vancouver: Vancouver School Board.
- APEGBC. (2011). Structural Engineering Guidelines for the Performance-based Seismic Assessment and Retrofit of Low-Rise British Columbia School Buildings - 1st Edition (SRG1). Burnaby, BC, Canada: Association of Professional Engineers and Geoscientists of British Columbia.
- APEGBC. (2017). *Structural Engineering Guidelines for the Performance-based Seismic Assessment and Retrofit of Low-Rise British Columbia Schools - 3rd Edition (SRG3)*. Burnaby: Association of Professional Engineers and Geoscientists of British Columbia.
- Ausenco. (2017). Lord Strathcona Elementary School - Heritage Classroom Building. *Canadian Consulting Engineering Awards 2017*. Vancouver: Association of Consulting Engineering Companies.
- Buckle, I. G., & Kelly, J. M. (1986). Properties of slender elastomeric isolation bearings during shake table studies of a large-scale model bridge deck. *Publication SP-94*, 247-269.
- Buckle, I. G., & Liu, H. (1993). Stability of Elastomeric Isolation Systems. *Proc., Seminar on Seismic Isolation, Passive Energy Dissipation, and Control* (pp. 293-305). Redwood City: Applied Technology Council.
- Buckle, I. G., & Liu, H. (1994). Experimental determination of critical loads of elastomeric bearings at high shear strain. *NCEER Bulletin*, 8(3), 1-5.
- Buckle, I., Nagaarajaiah, S., & Ferrel, K. (2002). Stability of elastomeric isolation bearings: Experimental study. *Journal of Structural Engineering*, 128(1):3-11.
- Chang, C. H. (2002). Modeling of laminated rubber bearings using an analytical stiffness matrix. *International Journal of Solids Structures*, 39(24), 6055-6078.
- Chen, M., Pantoli, E., Wang, X., Astroza, R., Ebrahimian, H., Hutchison, T., & Conte, J. P. (2016). Full-scale structural and nonstructural building system performance during earthquakes - Part I - Specimen description, test protocol, and structural response. *Earthquake Spectra*, 32(2), 737-770.
- Crowder, A., & Becker, T. (2017). Investigating substructure flexibility in column-top isolation systems with elastomeric bearings. *Journal of Structural Engineering*, 143(7).
- Freyssinet. (1954). *France Patent No. 1.110.285*.
- Gent, A. N. (1964). Elastic stability of rubber compression springs. *Journal of Mechanical Engineering and Science*, 6(4), 318-326.

- Government of British Columbia. (2019). *Seismic Mitigation Program*. Retrieved from Capital Management.
- Han, X., & Warn, G. P. (2014). Mechanistic Model for simulating critical behavior in elastomeric bearings. *Journal of Structural Engineering*, 141(5), 401-414.
- Haringx, J. A. (1949). *On highly compressible helical springs and rubber rods, and their application for vibration-free mountings, III*. Philips Research Reports.
- He, W. F. (2012). Nonlinear rotation and shear stiffness theory and experiment research on rubber isolators. *Journal of Engineering Mechanics*, 138(5), 441-449.
- Iizuka, M. (2000). A macroscopic model for predicted large-deformation behaviours of laminated rubber bearings. *Engineering Structures*, 22(4), 323-334.
- Insurance Bureau of Canada. (2016). *Study of impact and the the insurance and economic cost of a major earthquake in British Columbia and Ontario/Quebec*. Toronto: Air Worldwide.
- Ishii, K., Kikuchi, M., Nishimura, T., & Black, C. J. (2017). Coupling behaviour of shear deformation and end rotation of elastomeric seismic isolation bearings. *Earthquake Engineering & Structural Dynamics*, 46, 677-694.
- Kalpakidis, I. V., Constantinou, M. C., & Whittaker, A. S. (2010). Modeling strength degradation in lead-rubber bearings under earthquake shaking. *Earthquake Engineering and Structural Dynamics*, 39(13), 1533-1549.
- Karbaksh Ravari, A. O.-M. (2012). P-Delta and end rotation effects on the influence of mechanical properties of elastomeric isolation bearings. *Journal of Structural Engineering*, 138(6), 669-675.
- Kelly, J. M. (1997). *Earthquake resistant design with rubber* (2nd ed.). New York: Springer Verlag.
- Kelly, J. M., & Konstantinidis, D. A. (2011). *Mechanics of Rubber Bearings for Seismic and Vibration Isolation*. West Sussex: John Wiley & Sons Ltd,.
- Kikuchi, M., Nakamura, T., & Aiken, I. (2010). Three-dimensional analysis for square seismic isolation bearings under large shear deformations and high axial loads. *Earthquake Engineering and Structural Dynamics*, 39(13), 1513-1531.
- Koh, C. G., & Kelly, J. M. (1987). *Effects of axial load on elastomeric isolation bearings*. Berkeley: Earthquake Engineering Research Center.
- Koh, C. G., & Kelly, J. M. (1988). A simple mechanical model for elastomeric bearings used in base isolation. *International Journal of Mechanical Science*, 30(12), 933-943.
- Kumar, M., & Whittaker, A. C. (2014). An advanced numerical model of elastomeric seismic isolation bearings. *Earthquake Engineering & Structural Dynamics*, 43(13), 1955-1974.

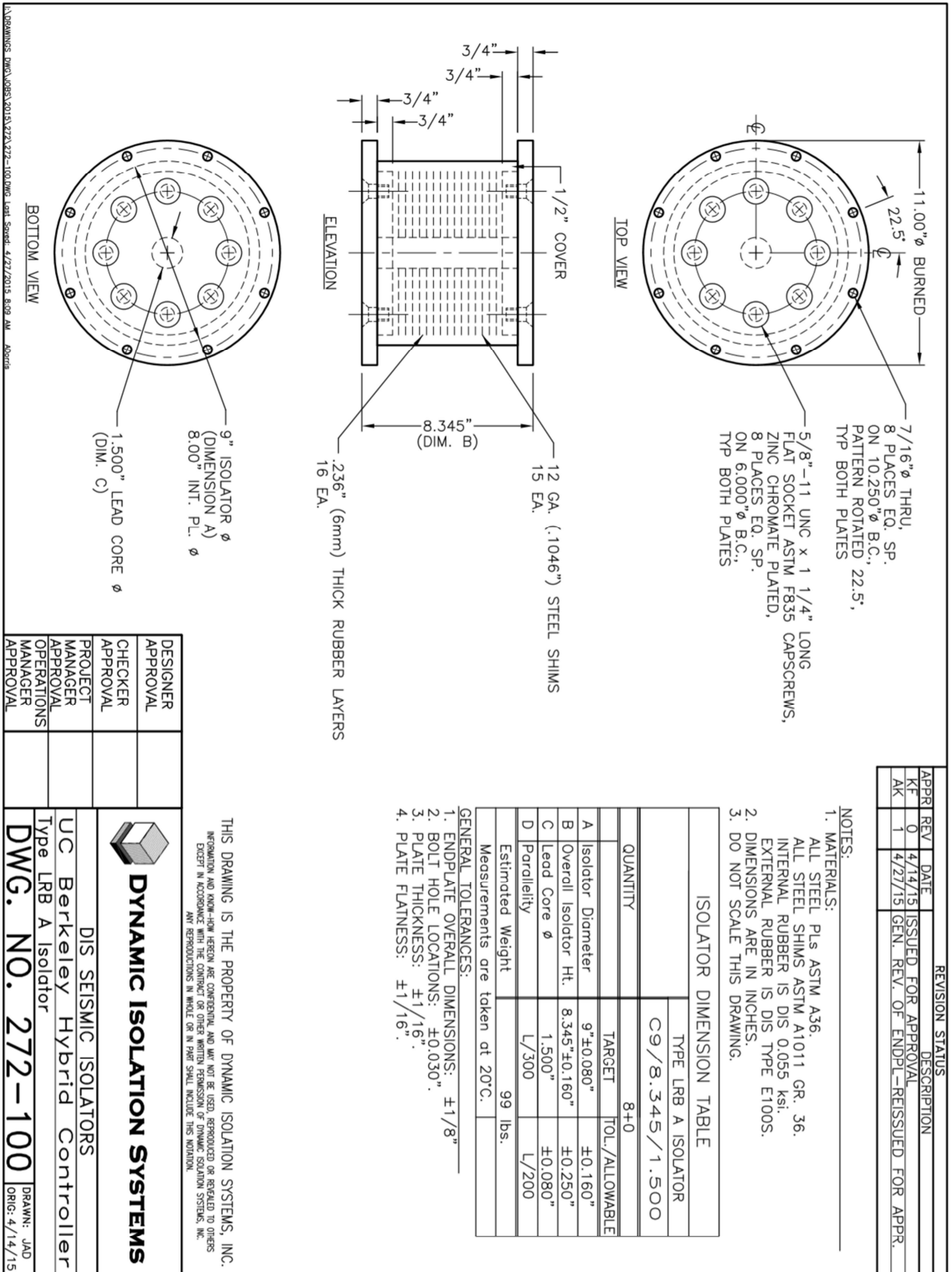
- Kumar, M., Whittaker, A., & Constantinou, M. (2015). Response of base-isolated nuclear structures to extreme earthquake shaking. *Nuclear Engineering and Design*, 295, 860-874.
- Kunnath, S., Hoffmann, G., & Reinhorn, A. (1995). Gravity-load-designed reinforced concrete buildings - Part I: seismic evaluation of existing construction. *ACI Structural Journal*, 92(3):343-345.
- Kurucz, J. (2018). Seismic upgrade of Lord Strathcona elementary a Canadian first. *Vancouver Courier*. Vancouver, Canada.
- Matsagar, V., & Jangid, R. (2008). Base isolation for seismic retrofitting of structures. *Practice Periodical on Structural Design and Construction*, pp. 13(4):175-185.
- McKenna, F., & Fenvez, G. L. (2006). Open System for Earthquake Engineering Simulations. Pacific Earthquake Engineering Research Center.
- Nagarajaiah, S., & Ferrell, K. (1999). Stability of Elastomeric Seismic Isolation Bearings. *Journal of Structural Engineering*, 946-954.
- Naiem, F., & Kelly, J. (1999). *Design of Seismic Isolated Structures, 1st ed.* New York: John Wiley & Sons, Inc.
- NRCC. (2015). *National Building Code of Canada*. Ottawa: National Research Council of Canada.
- Pan, P., Zamfirescu, D., Nakashima, M., Nakayasu, N., & Kashiwa, H. (2005). Base-Isolated Design Practice in Japan: Introduction to the Post-Kobe Approach. *Journal of Earthquake Engineering*, 9(1), p.147-171.
- Pettinga, D., & Oliver, S. (2015). Aspects of design for the base isolated christchurch justice and emergency services precinct. *10th Pacific Conference on Earthquake Engineering*, (pp. 1-8). Sydney.
- Rastgoo Moghadam, S. (2017). Effect of support rotations on the behaviour of elastomeric bearings (Doctoral Dissertation). Hamilton, Canada: McMaster University .
- Rastgoo Moghadam, S., & Konstantinidis, D. (2017). Simple mechanical models for the horizontal behaviour of elastomeric bearings including the effects of support rotation. *Engineering Structures*, 150, 996-1012.
- San Francisco Public Works. (n.d.). *San Francisco City Hall Seismic Upgrade*. Retrieved from San Francisco Public Works: <https://www.sfpublishworks.org/cityhall>
- Sanchez, J., Masroor, A., Mosqueda, G., & Ryan, K. (2013). Static and Dynamic Stability of Elastomeric Bearings for Seismic Protection of Structures. *Journal of Structural Engineering*, 1943-1951.

- Sherstobitoff, J. (2018). Principal of the Seismic Group, Ausenco. (P. Communication, Interviewer)
- Skinner, R. I., Robinson, W. H., & McVerry, G. H. (1992). *An Introduction to Seismic Isolation*. West Sussex: John Wiley & Sons, Ltd.
- Stanton, J. F., Scroggins, G., Taylor, A., & Roeder, C. W. (1990). Stability of laminated elastomeric bearings. *Journal of Engineering Mechanics*, 116(6), 1351-1371.
- Tamura, K., Nakamura, Y., & Saito, T. (2004). A new base-isolated long-span structure overhanging urban infrastructure. *Council on Tall Buildings and Urban Habitat: Seoul Conference*, (pp. 1-17). Seoul.
- The Japan Society of Seismic Isolation. (2018). Number of SI Buildings in Japan, by Year. Japan: The Japan Society of Seismic Isolation.
- Vancouver School Board. (2019). *Long Range Facilities Plan*. Vancouver: City of Vancouver.
- Ventura, C., Finn, W., Bebamzadeh, A., & Pina, F. T. (2017). Seismic Retrofit of School Buildings in British Columbia, Canada. *16WCEE*. Santiago.
- VSU. (2019). *Long Range Facilities Plan*. Vancouver: Vancouver School Board.
- Warn, G., Whittaker, A., & Constantinou, M. C. (2007). Vertical Stiffness of Elastomeric and Lead-Rubber Seismic Isolation Bearings. *Journal of Structural Engineering*, 133, 1227-1236.

APPENDIX A: BEARING MANUFACTURER'S DRAWINGS

A.1: Bridgestone Natural Rubber Bearing

A.2: Dynamic Isolation Systems Lead Rubber Bearing



APPENDIX B: TEST SCHEDULE

Test Number	Date	Bearing Type	Column Type	Loading Type	Axial Load (kN)	Max Top Rotation (rad)
1	June 26, 2019	NRB	127x127	cyclical	100	0
2	June 26, 2019	NRB	127x127	cyclical	100	0.01
3	June 26, 2019	NRB	127x127	cyclical	100	0.02
4	June 26, 2019	NRB	127x127	cyclical	50	0
5	June 26, 2019	NRB	127x127	cyclical	50	0.01
6	June 26, 2019	NRB	127x127	cyclical	50	0.02
7	July 3, 2019	NRB	102x102	cyclical	50	0
8	July 8, 2019	NRB	102x102	cyclical	50	0.01
9	July 8, 2019	NRB	102x102	cyclical	50	0.02
10	July 8, 2019	NRB	102x102	cyclical	100	0
11	July 8, 2019	NRB	102x102	cyclical	100	0.01
12	July 8, 2019	NRB	102x102	cyclical	100	0.02
13	July 11, 2019	NRB	76x76	cyclical	50	0
14	July 11, 2019	NRB	76x76	cyclical	50	0
15	July 11, 2019	NRB	76x76	cyclical	50	0.01
16	July 11, 2019	NRB	76x76	cyclical	50	0.02
17	July 22, 2019	NRB	76x76	cyclical	100	0
18	July 22, 2019	NRB	76x76	cyclical	100	0
19	July 22, 2019	NRB	76x76	cyclical	100	0.01
20	July 22, 2019	NRB	76x76	cyclical	100	0.02
21	July 26, 2019	NRB	127x127	Cyclical	50	0.02
22	July 26, 2019	NRB	127x127	cyclical	100	0.02
23	August 9, 2019	LRB	76x76	cyclical	50	0
24	August 9, 2019	LRB	76x76	cyclical	50	0
25	August 9, 2019	LRB	76x76	cyclical	50	0.01
26	August 13, 2019	LRB	127x127	cyclical	50	0
27	August 14, 2019	LRB	127x127	cyclical	50	0.01

28	August 14, 2019	LRB	127x127	cyclical	50	0
29	August 14, 2019	LRB	127x127	cyclical	80	0
30	August 14, 2019	LRB	127x127	cyclical	80	0.01
31	August 14, 2019	LRB	127x127	cyclical	50	0.01
32	August 14, 2019	LRB	127x127	cyclical	80	0.01
33	August 20, 2019	LRB	102x102	cyclical	50	0
34	August 20, 2019	LRB	102x102	cyclical	50	0.1
35	August 20, 2019	LRB	102x102	cyclical	80	0
36	August 20, 2019	LRB	102x102	cyclical	80	0.01
37	Sept 3, 2019	NRB	127x127	stability	140	0
38	Sept 3, 2019	NRB	127x127	stability	160	0
39	Sept 3, 2019	NRB	127x127	stability	180	0
40	Sept 3, 2019	NRB	127x127	stability	200	0
41	Sept 3, 2019	NRB	127x127	stability	220	0
42	Sept 6, 2019	NRB	102x102	stability	140	0
43	Sept 6, 2019	NRB	102x102	stability	160	0
44	Sept 6, 2019	NRB	102x102	stability	180	0
45	Sept 6, 2019	NRB	102x102	stability	200	0
46	Sept 6, 2019	NRB	102x102	stability	220	0
47	Sept 9, 2019	NRB	127x127	half cycle	100	0

APPENDIX C: INSTRUMENTATION AND EQUIPMENT

Device	Manufacturer	Model
SDOF Load Cell	Interface	1020
6DOF Load Cell	TE Connectivity	FN7325-M16
Bottom plate inclinometer	Measurement Specialties	NS-5/DMG2-U
Vertical load actuator	Shur-Lift	4x18 Utility
Horizontal actuator	Shur-Lift	2.5x12 Implement
Rotation actuators	Enerpac	RSM-500
Linear sliders	THK	SHS30LC+1000L
Data acquisition	Agilent	34970A
Control system	MTS	FlexTest GT